Refinement of Antideuteron Formation Models

By

Raphael Wagner

A master thesis submitted to

the University of Oslo

for the degree of

MASTER OF SCIENCE

Faculty of Mathematics and Natural Sciences

University of Oslo

May 2020

Acknowledgement

I want to thank my supervisor Are Raklev for making this project possible. I am also very grateful for all the help and advise I got from Are, especially when it comes to writing down the thesis.

I also want to thank the ALICE collaboration for providing the measurements needed in this thesis.

Abstract

Anti-deuterons are a possible candidate for indirect detection of dark matter. In this thesis formation models of anti-deuterons are studied. The standard coalescence model and an empirically based cross-section model both can not well describe the anti-deuteron measurements from the LHC. We re-weight the nucleon input spectra based on experimental results from the LHC, and show that the compatibility improves drastically. Also a new space-time model, based on the distance of closest approach of the proton–neutron pairs is studied and gives good fits to the measurements. Finally, we investigate for the first time formation models in terms of measurements differential in multiplicity classes in order to search for signs of (anti)deuteron production directly from (anti)quark coalescence in high-multiplicity events. Also anti-deuteron production at 13 TeV is studied the first time.

Contents

Chapter 1

Introduction

In this thesis a selection of formation models of (anti-)deuterons are studied. Providing a good description of anti-deuteron formation is important because cosmic-ray anti-deuterons can be used as an indirect detection method for dark matter. Planned and ongoing experiments such as the BESS-Polar II, AMS-02 and GAPS experiments will provide measurements of cosmic-ray anti-deuterons or provide upper limits on the flux. Therefore accurate formation models of anti-deuterons are important to constrain various dark matter models. The data used to fit the free parameters of the formation models were provided by the ALICE experiment at the Large Hadron Collider at centre-of-mass energies of 0.9 TeV, 2.76 TeV, 7 TeV and for the first time data at 13 TeV has been studied. A re-weighting based on the measurements of protons and anti-protons has been used to improve the formation models. Also for the first time the multiplicity dependent anti-deuteron spectra at 7 TeV and 13 TeV are studied. Finally also a new formation model is studied which includes the space-time distributions of the neutrons and protons.

The thesis starts with a motivation for studying anti-deuteron formation models in chapter 2. The measurements used to fit the parameters of the models are described in chapter 3. In chapter 4 the phenomenological standard coalescence model and the more sophisticated cross-section formation model are described. To improve

the models the input proton and neutron spectra have been re-weighted on the basis of measurements. This is described in chapter 5. To study the possible impact of direct hadronisation for anti-deuterons, spectra differential in multiplicity are studied in chapter 6. Chapter 7 discusses the correlation of position and momentum of the proton–neutron spectra. A new space-time formation model for anti-deuterons is introduced and fitted to the data provided by the ALICE experiment. Finally in chapter 8 we draw conclusions from all the studied models.

Chapter 2

Dark Matter

Dark matter is one of the strongest indications for physics beyond the Standard Model (SM). In this chapter we will give a brief overview of the evidence of dark matter, how dark matter is searched for and how anti-deuterons can be used in experiments to detect dark matter.

2.1 Evidence for Dark Matter

The first evidence for dark matter came from astronomical observations of missing mass from the kinematics of the observed systems. J. H. Oort postulated the presence of dark matter in the Milky Way in 1932 after studying the velocities of stars near the galactic plane, by using Doppler shift [1]. Also F. Zwicky concluded in his work in 1933 that the visible luminous matter of the Coma cluster can not explain the observed velocity dispersion [2].

While dark matter was independently discovered at both galaxy and cluster scales in the early 1930s, the connection between the two was not drawn until much later in the 1970s as the hypothesis of dark matter was generally received by skepticism. Modern experiments use X-ray observations of virialized intracluster gas in combination with gravitational lensing to obtain far more accurate measurements

of the masses of galaxy clusters. Also numerical and theoretical studies support the evidence of dark matter. Mass configurations distributed in the galactic plane turned out to be unstable and should collapse towards a bar shape on cosmologically short time scales. By studying N-body simulations, J. P. Ostriker and P. J. E. Peebles found that this problem can be solved by additional unseen mass distributed as a spherical halo component [3]. Measurements of galactic rotation curves from spiral galaxies whose rotation axis is normal to the line of sight, performed by V. Rubin, are the strongest evidence for dark matter [4]. The observations show that the rotation curves which would be expected from the visible matter should drop quickly at large radii. However, the measured rotation curves typically flatten at these radii.

The above mentioned observations lead to the conclusion that dark matter is non-baryonic, however, the strongest evidence for its exotic nature comes from cosmological measurements of the Cosmic Microwave Background (CMB) and Baryon Acoustic Oscillations (BAO). The CMB is the relic radiation from the time of recombination, when the fully ionized baryonic matter in the universe started forming neutral atomic states. At this time the universe went under a transition from being opaque to becoming transparent to radiation.

Before the time of recombination, the photons and ionized baryons were coupled in a baryon–photon fluid. In the time after inflation, initial density perturbations in the dark matter density would grow due to gravitational attraction, and the baryon–photon fluid would fall into the resulting gravitational wells. While the baryon–photon fluid falls into the gravitational wells it creates a region of over-pressure and over-density. This causes an outgoing acoustic spherical wave. The gravitational attraction slows down the expansion and causes the system to re-collapse. This process refers to baryon acoustic oscillations. During the time of recombination the photons de-coupled from the baryons, which allowed the photons to escape and to produce the CMB we observe today. The baryons on the other hand did then no longer undergo the radiation pressure and form spherical shells around

the dark matter density perturbations, which then collapsed and formed galaxies. The BAO give a strong evidence that dark matter can not be "hot", which refers to being relativistic as this would allow to escape the gravitational well and wash out the density perturbations. Since the BAO are necessary to explain large scale structures of the universe, dark matter should rather be "cold" or "warm" referring to being non-relativistic or borderline relativistic.

Since many observations and theoretical studies lead to the conclusion of the existence of dark matter, and cosmological measurements show that dark matter is roughly five times more present than ordinary baryonic matter [5, 6], physicists want to find out what dark matter is, which is discussed in the next section.

2.2 Dark Matter Candidates

The most studied candidates for dark matter are weakly interacting massive particles (WIMPs). WIMPs are a class of particles which interact with standard model particles through the weak force. Examples of WIMP dark matter candidates include the lightest neutralino in supersymmtric theories and the lightest Kaluza–Klein state in theories of extra dimensions. The masses of WIMPs used for dark matter candidates are considered to be near the weak scale $E_{\text{weak}} \sim 100\text{GeV}$ as this is the scale where new physics is expected due to the hierarchy problem of the Higgs mass.

WIMPs fall into the category of thermal dark matter. Thermal dark matter refers to the production mechanism in the early universe by standard model particles. Shortly after the Big Bang the production and destruction of dark matter proceeded at equal rates, through annihilation or decay processes. As the universe expands the temperature drops, and due to the decreasing energy of SM particles caused by the expansion, the production mechanism of dark matter particles becomes inefficient. The annihilation process of dark matter which produces SM particles remains and causes the dark matter density to decrease until the point where the annihilation

rate and the expansion of the co-moving frame are of similar magnitude at which point the production stops. This process is referred to as chemical freeze-out.

This freeze-out would lead to a dark matter relic today, which for a WIMP dark matter candidate with a mass near the weak scale is approximated to be given by [7]

$$\Omega_\chi h^2 = 0.1 \frac{3 \cdot 10^{-26} \mathrm{cm}^3 \mathrm{s}^{-1}}{\langle \sigma v \rangle}. \tag{2.1}$$

Here Ω_χ is the dark matter mass density given by $\Omega_\chi = \rho_\chi / \rho_{\mathrm{crit}}$, where ρ_{crit} is the critical density required for a flat universe, $h = H_0/(100\mathrm{km\ s^{-1}Mpc^{-1}})$, with $H_0 = 67.74 \pm 0.46 \mathrm{km\ s^{-1}Mpc^{-1}}$ [8] the Hubble parameter, which describes the present expansion rate of the universe and $\langle \sigma v \rangle$ as the thermal average of the dark matter annihilation cross-section. To get the dark matter relic density today an annihilation cross-section of $\langle \sigma v \rangle \approx 3 \cdot 10^{-26} \mathrm{cm}^3 \mathrm{s}^{-1}$ is required. From a dimensional analysis it is possible to estimate a "natural" value of this cross-section as $\langle \sigma v \rangle \approx \alpha_w^2 / E_{\mathrm{weak}}^2 \approx 10^{-25} \mathrm{cm}^3 \mathrm{s}^{-1}$, where $\alpha_w \approx 1/29.5$ is the weak fine structure constant and $E_{\mathrm{weak}} \approx 100$ GeV is the weak scale. The coincidence that a weakly interacting dark matter candidate naturally gives a relic density which is just one order of magnitude smaller that the observed value is referred to as "WIMP miracle".

If dark matter was in chemical equilibrium in the early universe and froze-out due to expansion, dark matter particles should be able to interact with SM particles. This leads to different types of experiments to detect dark matter, discussed in the next section.

2.3 Dark Matter Detection

In this thesis anti-deuteron formation models are studied. Anti-deuterons consists of bound states of one anti-proton and one anti-neutron. These particles were first identified in the early 1960s in proton beams of the CERN Proton Synchrotron [9] and Brookhaven Alternating Gradient Synchrotron [10]. Deuterons which consist of

one proton and one neutron are naturally occurring and form an isotope of hydrogen. However, the production of both these particles in experiments allows to study the models of their formation [11, 12]. These production models consist of a two-stage formation process, with first the production of a nuclear cascade within which several nucleons then interact to form a (anti-)nucleus.

Anti-deuterons are particularly interesting because the flux prediction of anti-deuterons from the interaction of SM particles in cosmic rays is extremely low. This was first pointed out in ref.[13]. Therefore, anti-deuterons in cosmic-rays produced in dark matter annihilation or decay are an ideal candidate for indirect detection of dark matter.

To search for dark matter different types of searches can be combined, which are shown in figure 2.1.

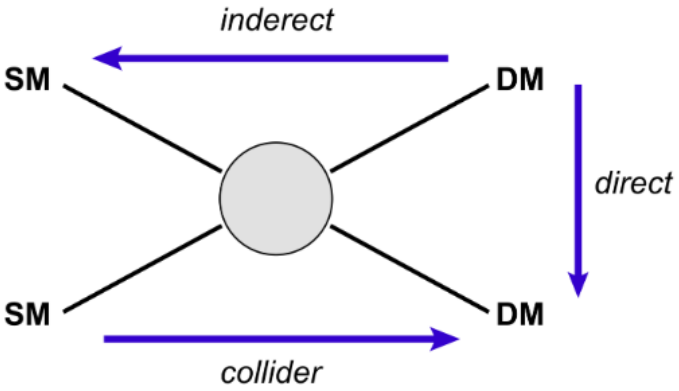

Figure 2.1: Dark Matter detection methods [14]

Looking at figure 2.1 from top to bottom shows direct searches in which dark matter interact with SM particles. This would be noticeable as a recoil of the SM particle coming from an invisible source. The second method reading from left to right used to search for dark matter are collider experiments. By the interaction of SM particles, dark matter particles could be produced which, would lead to missing energy in the event from the non-interacting dark matter. The third method is from left to right the indirect search by looking for products of dark matter annihilation or decays. Dark matter particles should be able to produce SM particles in collisions if

dark matter was in thermal equilibrium in the early universe and froze out later due to expansion. Decaying or annihilating dark matter therefore could produce anti-deuterons. Anti-deuterons coming from SM particles typically have a very large energy as seen in figure 2.2, due to the high threshold of the production mechanism ($\simeq 17 m_N$ in proton–proton collisions, where m_N is the nucleon mass).

Different experiments have been established to measure the anti-deuteron flux. Those include the BESS-Polar II, AMS-02 and GAPS, which are described in the following section.

2.4 Cosmic-ray Anti-deuteron Experiments

The recent best upper limit on the flux of cosmic-rays anti-deuteron is provided by the BESS Antarctic flight programme [15]. This limit was updated with the data of the BESS-Polar II measurements, presented at the International Cosmic Ray Conference [16]. The AMS-02 experiment is a spectrometer currently collecting data on the international space station, while the GAPS is a planned balloon-borne experiment, designed to measure the anti-proton and anti-deuteron flux specifically at low energy. The current and projected limits of these experiments are shown in figure 2.2 together with the predicted anti deuteron flux coming from different models which provide dark matter candidates.

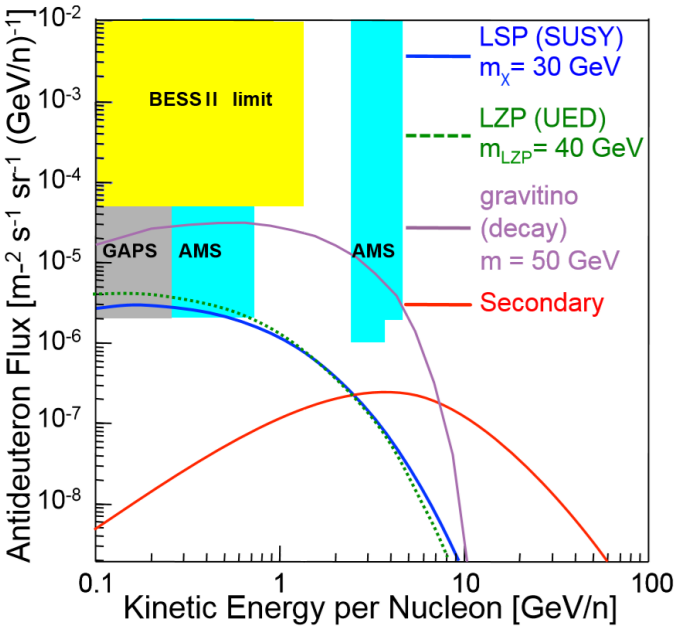

Figure 2.2: Predicted antideuteron flux as a function of kinetic energy per nucleon for a 30 GeV neutralino, a 40 GeV extra-dimensional Kaluza–Klein neutrino, and a 50 GeV gravitino. The red line is the expected flux coming from the standard model. The antideuteron limits from BESS II are shown, along with the projected sensitivities of AMS-02 for the superconducting-magnet configuration after 5 years of operation and GAPS after three 35-day flights. Taken from [17].

In the upcoming years the AMS-02 and the GAPS experiments should either give the first measurements of the anti-deuteron flux in cosmic-rays or provide even better upper limits which can be used to constrain the dark matter models. In order to use these measurements or upper limits to constrain dark matter models an accurate description of anti-deuteron formation is needed. Uncertainties in the formation models would lead to wrong conclusions in constraining the dark matter models. The correct tuning of the formation models has a significant influence on the average number of anti-deuterons produced and on the kinematics which determine the shape of the produced spectra. Both of these effects can change the predicted flux shown in figure 2.2. On the other hand also the propagation models which are needed to calculate the predicted anti-deuteron flux are a big uncertainty.

Recently published results of the anti-deuteron flux in cosmic-rays calculated

with an alternative coalescence model based on the Wigner-function as representation for the anti-nucleon and anti-nuclei states show that for an optimistic assumption of the dark matter and propagation parameters the predicted flux of anti-deuterons in cosmic-rays can be close to the sensitivity of GAPS ($2 \cdot 10^{-6}$ [m^{-2} s^{-1} sr^{-1}(GeV/n)$^{-1}$]) and AMS-02 (10^{-6} [m^{-2} s^{-1} sr^{-1}(GeV/n)$^{-1}$]) [18].

2.4.1 BESS-Polar II

The first run of the BESS-Polar experiment was done in Antarctica in 2004. This provided a first upper limit on the anti-deuteron flux coming in cosmic-rays [19]. The BESS-Polar II experiment was carried out in December 2007 to January 2008. In the BESS-Polar II experiment no anti-deuterons were observed as well, therefore these measurements provided an even harder upper limit on the flux as shown in figure 2.2.

The BESS-Polar II experiment identifies anti-matter by using a solenoidal magnetic field to identify charge and momentum. This magnetic field is filled by inner drift chambers and surrounded by aerogel Cherenkov counters and a time-of-flight system.

To identify anti-deuterons over the background which is mostly anti-protons but also electrons, muons and pions reliable measurements of the rigidity[1], velocity (β), and energy loss in the detector (dE/dx) is required. Relativistic electrons, muons, pions and anti-protons are rejected by the Cherenkov counters by measuring simultaneously velocity and momentum. The remaining particles are then identified by their specific energy loss in the detector. Events remaining after the cuts from the Cherenkov counters and dE/dx measurements are then studied by the measured mass. The mass is calculated by $m = ZR\sqrt{1/\beta^2 - 1}$ using the information about the charge Z, the rigidity R and the velocity β. The combination of these measurements excluded any possible signal of anti-deuterons within the detectors limits in anti-

[1] Rigidity is defined as $R = p/Z$, where p is the momentum and Z is the charge

deuteron energy.

2.4.2 AMS-02

The AMS-02 is taking data on the International Space Station (ISS) since 2011 [20]. It is designed as a general high-energy particle detector to measure electrons, positrons, protons, anti-protons, deuterons, anti-deuterons and even heavier nuclei like helium and anti-helium coming in cosmic-rays. The particles are identified by the tracking of charged particles in a magnetic field, measuring the velocity in a time-of-flight system and energy loss measurements. The deuterons are identified by calculating the particles mass in the same way as mention above in the BESS-Polar II experiment. As for the BESS-Polar II experiment also for the AMS-02 experiment, anti-protons give the biggest background that needs to be rejected. For doing that a rejection factor of 10^4–10^6 is required. To distinguish anti-protons from anti-deuterons very accurate measurements of the masses are necessary. Other backgrounds like electrons, positrons, protons and deuterons can easily be excluded due to their lower mass and/or opposite charges. The shown sensitivity of the anti-deuteron flux is based on the analysis done during the development phase, and was based on superconducting magnets. However, the detector has been launched with a normal magnet instead. The effect on the sensitivity is currently unknown.

2.4.3 GAPS

The GAPS experiment is a balloon-borne experiment designed specifically for measuring the anti-proton and anti-deuteron flux at low energy. The BESS-Polar II and AMS-02 experiments use a magnetic spectrometer to distinguish particles and anti-particles. The GAPS experiment uses a completely different approach. The detector consists of layers of semi-conducting Si targets in an Al frame. An anti-particle traveling through these layers will lose energy and at some point it will be trapped in a nucleus of the Si layers or the Al frame. This will form an exotic

atom in an excited state. The exotic atom will de-excite by emitting X-rays of a characteristic energy and then annihilate on the target nucleus by producing a shower of pions and baryons. To identify the particles trapped in the detector the X-ray energies, the annihilation product multiplicity, the energy loss in the detector dE/dx and the stopping depth is used. Anti-protons with the same velocity as an anti-deuteron will penetrate less deeply, produce a different X-ray signature and will produce fewer annihilation products. This method of identifying particles gives a reliable rejection to any non-anti-matter particles.

The design of the GAPS experiment is finished and a prototype GAPS payload was constructed and tested from the Taiki Aerospace Research Field in Japan in 2012 [21]. The test of the prototype was successful as all engineering and science goals of the flight were satisfied.

As shown in figure 2.2 the energy range of GAPS and AMS-02 are mostly complementary. However, there is a small overlap at the low energy range of the AMS-02 experiment with GAPS. In case the AMS-02 experiment has observed cases of anti-deuterons a complementary experiment like GAPS is needed for confirmation, as detecting anti-deuterons in cosmic-rays is a rare event search.

Chapter 3

Anti-deuteron Measurements in ALICE

3.1 Particle Identification and Triggering

The ALICE detector [22] is designed to study heavy-ion collisions, and light nuclei and anti-nuclei in proton-proton collisions at the LHC.

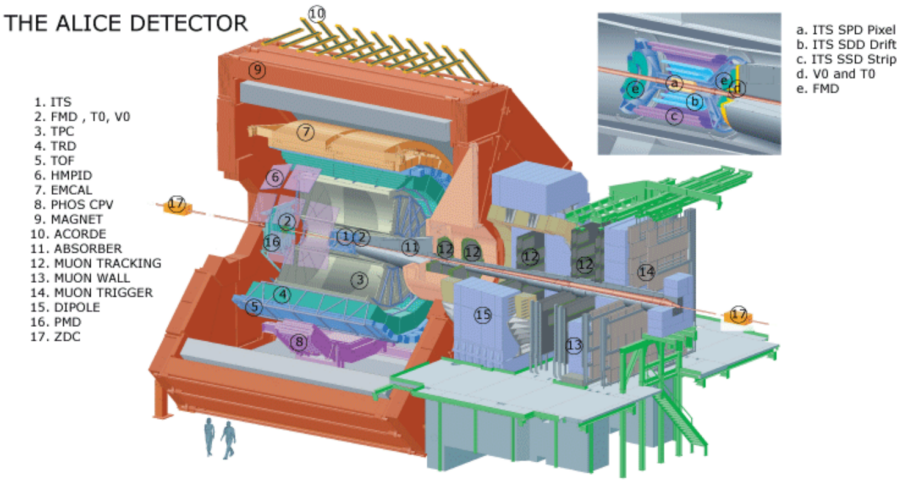

Figure 3.1: The ALICE detector at the LHC [23].

For the measurement of the anti-deuteron and anti-proton spectra used in this

thesis the central detectors of ALICE have been used for particle identification. These detectors are the inner tracking system (ITS), the time projection chamber (TPC) and the time-of-flight (TOF) detector, which can be seen in figure 3.1: 1, 3, 5. The detectors are all located inside a solenoidal magnetic field of 0.5 T. All three detectors cover the full azimuth in a pseudo-rapidity region of $|\eta| < 0.9$[1]. Anti-deuterons are measured at mid-rapidity $|y| < 0.5$[2], and to avoid edge effects a pseudo-rapidity cut of $|\eta| < 0.8$ was applied. However, since many nuclei at low p_T are inside $|y| < 0.5$ but outside $|\eta| < 0.8$, the number of anti-deuterons was extrapolated using MC simulations where the rapidity distribution was assumed to be flat [24, 25, 26]. This problem does not occur for the measurements of (anti-)protons due to their lighter mass they behave more relativistic in the same range of momentum. Therefore there is a smaller difference in rapidity and pseudo-rapidity for (anti-)protons.

The innermost detector used for tracking is the ITS [27] which consists of two layers of silicon pixel detectors (SPD), figure 3.1 a, followed by two layers of silicon drift detectors(SDD) ,figure 3.1 b, and two layers of double-sided silicon strip detectors(DSSD) ,figure 3.1 c. The ITS is mainly used for reconstructing the primary and secondary vertex of particle tracks. The silicon detectors have all a similar working principle. Particles which travel through the detector hit electrons out of nucleus. This creates freely moving positive (holes) and negative (electrons) charges, which drift towards the read out under the influence of an electric field. A SPD consists of an array of pixels, similar to a digital camera, in which each pixel has its own read out. In a SDD the charges drift towards a collection electrode. The read out of a DSSD consists of perpendicular strips on two sides of the detector, where each direction of strips can only determine the position of one co-ordinate.

The TPC [28] is the main tracking detector and consists of a hollow cylinder

[1]Pseudo-rapidity of a particle with momentum p is in experimental particle physics defined as $\eta = \frac{1}{2}\ln\left(\frac{|p|+p_z}{|p|-p_z}\right)$

[2]Rapidity of a particle with momentum p and energy E is in experimental particle physics defined as $y = \frac{1}{2}\ln\left(\frac{E+p_z}{E-p_z}\right)$

parallel to the beam pipe. The volume is filled with a $Ne/CO_2/N_2$ gas mixture, at atmospheric pressure. The gas is ionised by charged particles traversing the detector. The ionisation electrons drift towards the end-plates, under the influence of a constant electric field, where their positions and arrival times are measured to reconstruct particle tracks. The ITS combined with the TPC are used to measure the particle momenta.

To identify particles the specific energy loss measurement (dE/dx) in the TPC gas is used and combined with the momentum measurement. This energy loss can be described by the Bethe–Bloch formula.

$$-\frac{dE}{dx} = \frac{4\pi}{m_e}\frac{nZ^2}{\beta^2}\left(\frac{e^2}{4\pi\epsilon_0}\right)^2\left[\ln\left(\frac{2m_e\beta^2}{I(1-\beta^2)}\right) - \beta^2\right]. \tag{3.1}$$

Here E is the energy of the particle, x is the traveled distance, m_e is the electron mass, β is the velocity of the particle, ϵ_0 is the vacuum permittivity, n is the electron number density and I is the mean excitation potential of the gas. For particle identification, combined measurements from the TOF and TPC are used. Figure 3.2 shows the energy loss in the TPC (dE/dx) for particles with negative charges versus their rigidity. The different particles can be identified by their predicted behaviour in the non-relativistic region of the Bethe–Block function.

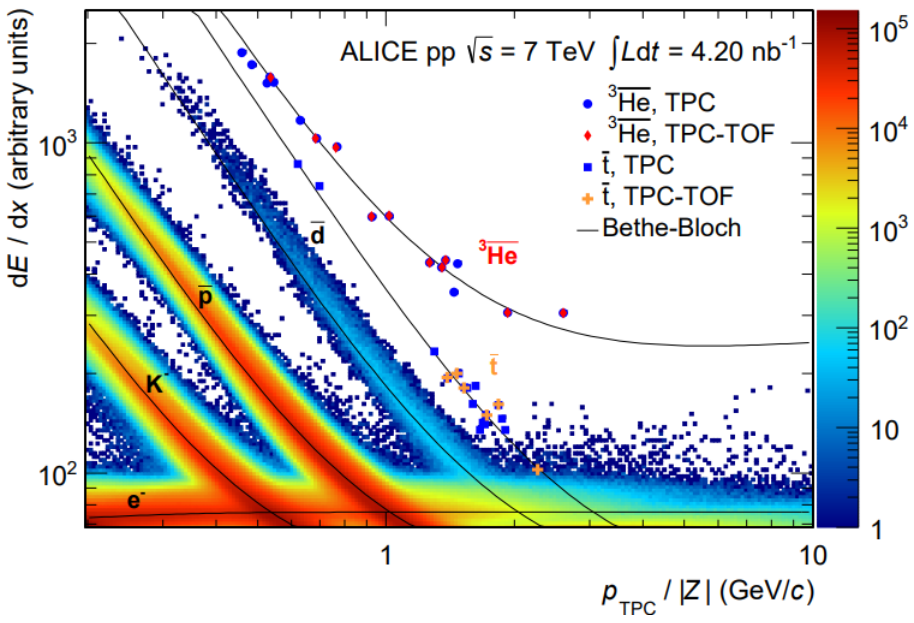

Figure 3.2: Energy loss in the TPC (dE/dx) versus the rigidity estimated at the TPC inner wall ($p_{TPC}/|Z|$). The solid lines represent the expected energy loss according to the parametrization of the Bethe-Bloch formula (3.1) [24].

The TOF [29] system is based on multi-gap resistive plate chambers measuring hit position and time of arrival, and is located with a cylindrical symmetry around the beam pipe. The particle identification in the TOF system is based on the difference between the measured time-of-flight and the expected value, evaluated for each mass hypothesis from track momentum and length.

For triggering the V0 detectors have been used [30], which can be seen in figure 3.1 d. The V0 detector consists of the V0A and V0C detectors which are located at the sides of the beam pipe and cover a pseudo-rapidity range of $2.8 < \eta < 5.1$ and -3.7 $< \eta <$ -1.7, respectively. The main task of these detectors is to select events coming from proton-proton interactions and reject events coming from beam-background interactions. In order to trigger on an event, charged particles need to hit both the V0A and V0C detectors. This also suppresses single-diffractive events as shown in figure 3.3 and discussed in the next section. The triggering is done by using the timing information of charged particles hitting the V0 detectors. This is illustrated in figure 3.3.

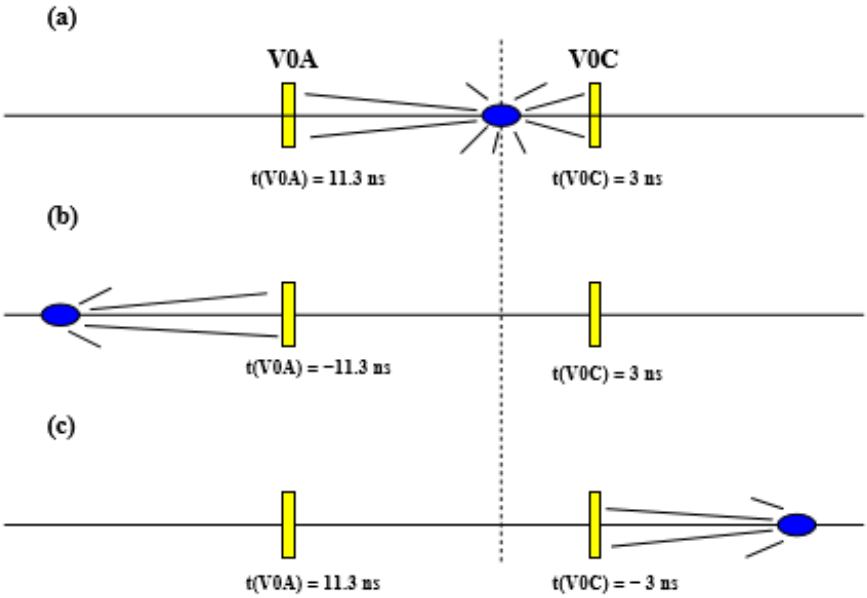

Figure 3.3: Illustration of different arrival times of beam-beam and beam-background interactions. In (a) the beam-beam interaction produces charged particles in the V0A and V0C detector at known times depending on the location of the primary vertex. In (b) and (c) the beam-background interaction produced charged particles which hit one of the V0 detectors earlier [30].

3.2 Normalizing the Simulated Events to Data

The deuteron and anti-deuteron measurements as well as the proton and anti-proton measurements in ALICE at the LHC have been performed at 0.9, 2.76, 7 and 13 TeV CoM energy [24, 25, 26]. The spectra used in this thesis are normalized either to non-single-diffractive (NSD), inelastic (INEL) or INEL>0 events, which are all INEL events with at least one charged particle in the pseudo-rapidity region $|\eta| < 1$. The INEL>0 events corresponds to approximately 75% of the total INEL cross section. INEL events contain non-diffractive (ND), single-diffractive (SD), central-diffractive (CD) and double-diffractive (DD) events. Different event types produce particles in different pseudo-rapidity regions. ND events are regular collisions which produce particles in all directions without a large rapidity gap. These events are almost equivalent to the minimum-bias component of the total cross section. Usually

minimum-bias refers to the experimental setup, while ND refers to the way events are generated in the MC generator. In a diffractive process the proton gets excited in colour and then decays into a small shower. In DD events both protons break up and produce a lot of particles in the forward and backward region with a large rapidity gap. In SD events only one of the protons break up which produces particles in the forward or backward region. CD events are not considered in this thesis since they have a very small cross-section and are turned off by in the default tuning of `PYTHIA 8`. The characteristics of INEL events are shown in figure 3.4.

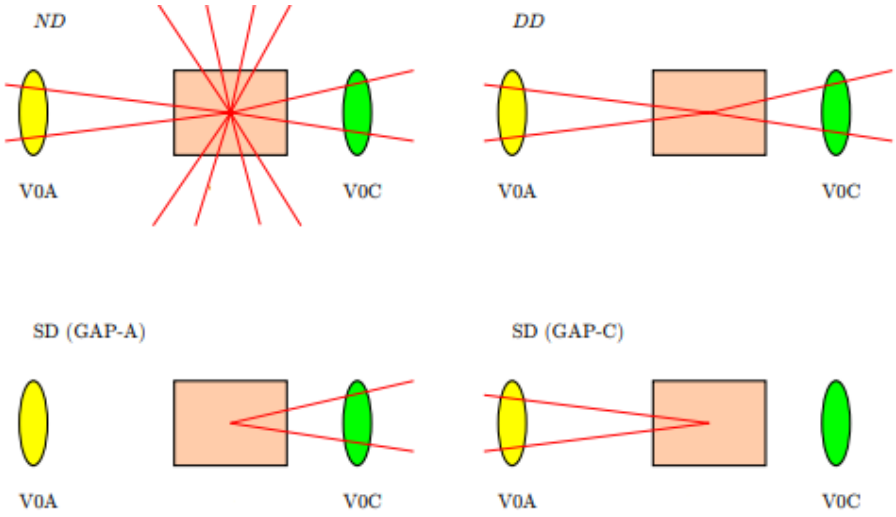

Figure 3.4: Types of INEL events in ALICE [31].

The measurements of anti-deuterons for 0.9, 2.76 and 7 TeV [24] in ALICE used mostly NSD (non single diffractive) events, since SD events are suppressed by the trigger mechanism. The results of the measurements have then been rescaled by the energy dependent factors of $0.763^{+0.022}_{-0.008}$, $0.760^{+0.052}_{-0.028}$, and $0.742^{+0.050}_{-0.020}$, respectively, in order to extrapolate to the total number of INEL events [32]. These numbers are calibrated from data. In the models implemented in `PYTHIA` used in this thesis only ND events contribute significantly to the anti-deuteron spectra measured in the mid region. Therefore only ND events are simulated in `PYTHIA` and then rescaled to INEL events. This means that the data is first rescaled from ND to NSD events and then from NSD to INEL.

Since the events generated by the event generators are only ND events, the final anti-deuteron spectrum is re-scaled by the fraction of triggered events that are ND. Which means [11]:

$$\frac{1}{2\pi N_{ev}} \frac{d^2N_d}{dp_T dy}\Big|_{\text{trig}} \simeq f_{ND,trig} \frac{1}{2\pi N_{ev}} \frac{d^2N_d}{dp_T dy}\Big|_{\text{ND}}, \tag{3.2}$$

where N_{ev} is the total number of events and N_d is the number of deuterons in these events. The number of triggered ND events compared to the number of total triggered events is given by:

$$f_{ND,trig} \equiv \frac{N_{ND,trig}}{N_{trig}} = \frac{\epsilon_{ND} N_{ND}}{\sum_i \epsilon_i N_i} = \frac{\epsilon_{ND} f_{ND}}{\sum_i \epsilon_i f_i}. \tag{3.3}$$

Here ϵ_i is the efficiency, N_i is the total number of events and f_i is the fraction of total events of the process type i. The subscript "trig" indicates events after trigger, the others are before trigger. The sum of total number of triggered events is over all inelastic processes: single-, double-, central- and non-diffractive. The trigger efficiencies have been calculated in [11] using `PYTHIA 6` and `PHOJET`. The results are shown in table 3.1

Energy/$f_{ND,trig}$	`Pythia 6`	`PHOJET`	Average
0.9 TeV	0.837	0.856	0.847
2.36 TeV	0.832	0.875	0.854
7 TeV	0.831	0.891	0.861

Table 3.1: Estimated fraction of minimum bias events that pass the ALICE V0AND trigger that are non-diffractive. Taken from [11].

For the simulations for 2.76 TeV CoM energy the results from 2.36 TeV have been used. For 13 TeV the ratios of the different INEL cross-section estimated in `PYTHIA` have been used for the normalizing, which are given in table 3.2.

Event type	σ [mb]
ND	56.42
$SD_{AB\rightarrow AX}$	6.416
$SD_{AB\rightarrow XB}$	6.416
DD	8.798
CD	0

Table 3.2: Fractions of INEL cross-sections estimated by `PYTHIA` for 13 TeV CoM energy.

The results from table 3.1 gives the re-scaling from ND to NSD events since SD events are not triggered. The measurements of anti-deuterons are presented normalized to INEL events therefore the NSD events need to be further normalized, where from NSD to INEL the same factors as mentioned above are used.

3.3 Extrapolating the Spectra

In order to extend the usability of the measured anti-proton transverse momentum spectra from ALICE, an appropriately parameterized function is needed to extrapolate into the unmeasured p_T region. Anti-proton spectra are measured at mid-rapidity ($|y| < 0.5$) and cover the transverse momentum range from 0.3 GeV up to 3 GeV.

In the past, exponential functions have been used to extrapolate spectra to the low p_T region, such as [33]:

$$\frac{1}{2\pi p_T}\frac{d^2N}{dydp_T} = Ae^{\frac{-m_T}{T}}, \tag{3.4}$$

with free fit parameters A, T and the transverse mass $m_T = \sqrt{p_T^2 + m_0^2}$. Here m_0 is the rest mass of the particle. The low p_T part must be described by nonperturbative QCD and attempts at theoretical models have been made involving the parton wave

functions in a flux tube [34], the thermodynamics and recombination of partons [35], or the fragmentation of a QCD string [36]. The high region of the p_T range can be described by perturbative QCD hard-scattering between two partons of different hadrons [37, 38]. This leads to QCD inspired power laws to describe the high p_T region ($p_T > 3$ GeV) [33], such as the Hagedorn distribution [39]:

$$E\frac{d^3\sigma}{dp^3} = C\left(1+\frac{p_T}{p_0}\right)^{-n}, \tag{3.5}$$

with free fit parameters C, p_0 and n. The left-hand side of eq.(3.4) and eq.(3.5) are related through:

$$E\frac{d^3\sigma}{dp^3} = \frac{d^3\sigma}{p_T d\phi dp_T dy} \rightarrow \frac{d^2\sigma}{2\pi p_T dy dp_T}. \tag{3.6}$$

In the first step we did a variable transformation to cylindrical co-ordinates and used the relation $dp_z/dy = E$, in the second step we averaged over ϕ because there is no preferred azimutal direction. The Hagedorn function converges to an exponential for small p_T and turns into a power law for high p_T:

$$\left(1+\frac{p_T}{p_0}\right)^{-n} \rightarrow \begin{cases} \exp\left(-\frac{np_T}{p_0}\right) & : p_T \rightarrow 0 \\ \left(\frac{p_0}{p_T}\right)^n & : p_T \rightarrow \infty \end{cases}. \tag{3.7}$$

This shows the relationship to eq. (3.4):

$$\begin{gathered} \frac{np_T}{p_0} \xrightarrow{p_T \rightarrow 0} \frac{m_T}{T} \\ C \rightarrow A \end{gathered} \tag{3.8}$$

The p_T coverage of the measurements used in this thesis are large enough to cover the low and high p_T regions.

In Relativistic Heavy Ion Collider (RHIC) and at the LHC experiments the transverse momentum spectra of charged particles have been measured and described by the Tsallis distribution [40, 41]:

$$h_q(p_T) = C_q\left[1-(1-q)\frac{p_T}{T}\right]^{\frac{1}{1-q}}, \tag{3.9}$$

with a fitted normalization C_q, a "temperature" T, and a dimensionless nonextensivity parameter q ($q > 1$). The parameter q provides a useful measure of intrinsic (non-statistical) fluctuations in the system.

The Tsallis distribution can be regarded as a nonextensive generalization of the exponential Boltzmann-Gibbs distribution and converges to it when the parameter q is close to unity.

$$h(p_T) \xrightarrow{q\to 1} C_1 e^{-\frac{p_T}{T}}. \tag{3.10}$$

Which is the same as the exponential function mentioned earlier in eq.(3.4) with the substitution $p_T \to m_T$ regulating the low energy tail when $p_T \to 0$. The Tsallis distribution has been very successfully in describing physical systems including multiparticle production processes at lower energies [42]. The Hagedorn and Tsallis distributions are equivalent under the relations:

$$n = \frac{1}{q-1} \quad \text{and} \quad p_0 = \frac{T}{q-1}. \tag{3.11}$$

While the two functions are equivalent from a phenomenological point of view, they come from a very different background as the Hagedorn function is empirically determined.

However, the best fits to the experimental spectra of particles are usually obtained by a modified function suggested by Lévy, called the Lévy-Tsallis distribution [43]:

$$\frac{1}{2\pi p_T N_{ev}} \frac{d^2N}{dp_T dy} = \frac{dN}{dy} \frac{1}{2\pi} \frac{(n-1)(n-2)}{nC(nC + m_0(n-2))} \left(1 + \frac{m_T - m_0}{nC}\right)^{-n}. \tag{3.12}$$

with free fit parameters n and C. The $\frac{dN}{dy}$ distribution is here assumed to be constant and must also be fitted to the experimental data. This functions gives a very good fit of the spectra over the entire measured range of p_T. In chapter 5 this function is used to extrapolate the measured spectra of anti-protons [31] mostly for the low p_T region, in order to re-weight the input spectra for the formation models.

Chapter 4

Coalescence Models

The formation models for compound nuclei and anti-nuclei in this thesis are always the same. Therefore the "anti" will be dropped from now on and whenever we speak of nuclei it stands for nuclei and anti-nuclei.

4.1 Standard Coalescence Model

The coalescence model is used to describe the formation of deuterons and antideuterons [44]. It is a phenomenological model where any proton–neutron pair form a deuteron if their momenta are close enough.

$$|p_p - p_n| < p_0. \tag{4.1}$$

Here p_p and p_n are the 4-momenta of the proton and neutron. This criterion is applied to each proton–neutron pair on a per event basis. In this form the formation criterion is Lorentz invariant. This semi classical model has only one free parameter which is p_0. To determine the value of p_0 it is necessary to calibrate simulations from event generators giving proton and neutron spectra to experimental data on deuterons. So far there is no consistent value of p_0 that fits all simulations and experiments. This could be caused by differences in the event generators, by the differences in the experiments or that this model is too simple.

In addition to the momentum criterion it is also necessary to take into account the spatial separation of the particles. Nuclear interactions are very short ranged while weakly decaying particles have much bigger, macroscopic, decay lengths. Therefore there is another condition for the formation of deuterons which treats particles with a lifetime of $\tau > 10^{-10}$mm/c as stable to exclude protons and neutrons coming from weak interactions.

When an neutron–proton pair forms a deuteron, the model describes a $2 \rightarrow 1$ process. Such a process does not preserve energy-momentum conservation. Usually this problem is solved by calculating the deuteron 3 momentum by:

$$\vec{p_p} + \vec{p_n} = \vec{p_d}. \tag{4.2}$$

Then determining the energy through the energy momentum relation:

$$E_d = \sqrt{|\vec{p_d}|^2 + m_d^2}. \tag{4.3}$$

This method implicitly assumes that the additional energy is lost. Another way to treat this problem is by considering a $2 \rightarrow 2$ process. This is described by $pn \rightarrow d\gamma$. In this radioactive capture process the deuteron is created in an excited state and emits a photon at a later point. For low centre-of-mass (CoM) momentum differences, which is required from the coalescence model, this is the main deuteron formation process. In that case the 4-momentum of the deuteron is given by:

$$p_p + p_n = p_d + p_\gamma. \tag{4.4}$$

And then taking into account the energy loss and change in momentum from the photon recoil at a later point. This describes a $2 \rightarrow 1$ process with a $1 \rightarrow 2$ decay and is simple to do in the centre of mass frame.

The algorithm used to take into account the recoil of the photon is described in section 4.3 where all process kinematics used in this thesis are described.

4.2 Cross Section Model

The coalescence model is fully deterministic, and the probability of an proton–neutron pair to form a deuteron can be expressed as a step function, because the coalescence criterion is given by eq. (4.1). In the centre of mass frame this would be:

$$p(pn \to d\gamma|k) = \theta(p_0 - k). \tag{4.5}$$

With $k = |\vec{p_p} - \vec{p_n}|_{\mathrm{CoM}}$. Since protons and neutrons are not classical objects, a better treatment would be a quantum mechanical description. Thus it might be better to replace the deterministic model by a phenomenological model where the probability of any proton–neutron pair to form a deuteron varies as a function of k. In a cross section based model from [11] the probability of a proton–neutron pair to form a deuteron is given by:

$$P(pn \to dX|k) = \frac{\sigma_{pn\to dX}(k)}{\sigma_0}. \tag{4.6}$$

Here $\sigma_{pn\to dX(k)}$ is the sum of the cross sections for all processes with pn as initial and dX as final state. The model has only one free parameter which is σ_0 which needs to be determined by calibrating against experimental data in the same way as the standard coalescence model. The processes considered in this model are not only $pn \to d\gamma$, which is the main process for low CoM energies. If the CoM energy is above the pion production threshold processes with extra hadronic final states become more important, which are $pn \to d(N\pi)^0$. At these energies also pp and nn processes with final states $d(N\pi)$ can contribute and have to be taken into account aswell. All processes considered in the model are summarized in table 4.1

1) $\bar{p}\bar{n} \to \bar{d}\gamma$	5) $\bar{p}\bar{p} \to \bar{d}\pi^-$
2) $\bar{p}\bar{n} \to \bar{d}\pi^0$	6) $\bar{p}\bar{p} \to \bar{d}\pi^-\pi^0$
3) $\bar{p}\bar{n} \to \bar{d}\pi^+\pi^-$	7) $\bar{n}\bar{n} \to \bar{d}\pi^+$
4) $\bar{p}\bar{n} \to \bar{d}\pi^0\pi^0$	8) $\bar{n}\bar{n} \to \bar{d}\pi^+\pi^0$

Table 4.1: Processes considered in the Cross Section Model [11].

Analog to eq. (4.6) the probability for any process to form a deuteron is given by:

$$P(N_1, N_2 \to dX_i|k) = \frac{\sigma_{N_1,N_2\to dX_i}(k)}{\sigma_0}. \tag{4.7}$$

In this case N_1, N_2 are the initial state nuclei and X_i are the final state particles in addition to the deuteron. For the processes considered in this model little or no data was available to perform fits for the desired cross sections for anti-deuterons [11]. In order to get the wanted cross section as a function of k it is assumed that the cross section for particles and anti-particles is the same $\sigma_{N_1,N_2\to d\overline{X}_i} = \sigma_{\overline{N}_1,\overline{N}_2\to \bar{d}X_i}$. The individual cross sections and kinematics of the final state particles are discussed in the subsequent subsections.

4.2.1 The $pn \to d\gamma$ Process

The process $pn \to d\gamma$ in this model is described by the function [11]:

$$\frac{\sigma_{pn\to d\gamma}(\kappa)}{(1\mu\text{b})} = \begin{cases} \sum_{n=-1}^{10} a_n \kappa^n & : \kappa < 1.28 \\ \exp(-b_1\kappa - b_2\kappa^2) & : \kappa \geq 1.28 \end{cases}, \tag{4.8}$$

where $\kappa = k/(1\text{ GeV})$. The exponential for high energies denies an unphysical divergent behaviour. Furthermore the probability is restricted by:

$$P(pn \to d\gamma|k) = \min\left(\frac{\sigma_{pn\to d\gamma}(\kappa)}{\sigma_0}, 1\right), \tag{4.9}$$

to take care of the κ^{-1} term for low energies. The free parameters of eq. (4.8) are determined by performing a least square fit to a set of experimental data which consists of contributions from the $pn \to d\gamma$ process and the inverse photo disintegration process $d\gamma \to pn$ [11]. These data sets can be combined by using the principle of detailed balance [45, 46] which relates the cross section of a process to the cross section of the inverse process:

$$\sigma(Aa \to Bb) = \frac{g_B g_b}{g_A g_a}\frac{p_b^2}{p_a^2}\sigma(Bb \to Aa), \tag{4.10}$$

where p_i is the momentum and g_i is the number of spin states for particle i. For massive particles this is $g_i = 2s_i + 1$. All quantities are given in the CoM frame. The best fit for the parameters of eq. (4.8) are shown in table 4.2

Parameter	Value	Parameter	Value
a_{-1}	2.30346	a_0	$-9.366346\ 10^1$
a_1	$2.565390\ 10^3$	a_2	$-2.5594101\ 10^4$
a_3	$1.43513109\ 10^5$	a_4	$-5.0357289\ 10^5$
a_5	$1.14924802\ 10^6$	a_6	$-1.72368391\ 10^6$
a_7	$1.67934876\ 10^6$	a_8	$-1.01988855\ 10^6$
a_9	$3.4984035\ 10^5$	a_{10}	$-5.1662760\ 10^4$
b_1	-5.1885	b_2	2.9196

Table 4.2: Best fit values for the parameters of eq. (4.8) [11]

If this process forms a deuteron the momentum can be calculated in the same way as the $2 \to 2$ process described in the standard coalescence model. The momentum of the final deuteron is determined by eq. (4.19) and the direction is drawn from a two-dimensional spherical uniform distribution in the CoM frame.

4.2.2 The $X_1, X_2 \to d\pi$ Processes

The cross sections of the $X_1, X_2 \to d\pi$ processes are related by isospin invariance [47] through:

$$\begin{aligned} \sigma_{pn\to d\pi^0} &= \frac{1}{2}\sigma_{pp\to d\pi^+} \\ \sigma_{nn\to d\pi^-} &= \sigma_{pp\to d\pi^+}. \end{aligned} \tag{4.11}$$

However these relations are not exact due to the slightly different nucleon and pion masses. The cross section for $pp \to d\pi^+$ is described by the function [48]:

$$\sigma_{pp\to d\pi^+} = \frac{a\eta^b}{(c - \exp(d\eta))^2 + e}. \tag{4.12}$$

Here $\eta = q/m_{\pi^+}$ and q is the momentum of the pion in the CoM frame. The parameters a, b, c, d, and e are determined by fitting the function to experimental data which was done in [48]. The best fit parameters can be seen in table 4.3

Parameter	Value
$a[\mu b]$	170
b	1.34
c	1.77
d	0.38
e	0.096

Table 4.3: Best fit values for the parameters of eq. (4.12) [48]

Further corrections should possibly be taken into account when using this fit combined with the isospin relations, as the fit was made in comparison to $pn \to d\pi^0$ data. Then the fit was corrected for Coulomb repulsion and phase space differences caused by different pion masses. However these effects are only important near the production threshold and are expected to shift the threshold only slightly. Since the production mechanism of deuterons should not be sensitive to the exact position of this threshold these corrections are neglected in the model. Below the production threshold the cross section is defined as zero. Also for this process the recoil of the emitted pion must be taken into account. This is done in exactly the same way as for the photon in the previous subsection. The momentum of the final deuteron is determined by eq. (4.19) and the direction is again drawn from a two-dimensional spherical uniform distribution in the CoM frame.

4.2.3 The $2 \to 3$ Processes

The $2 \to 3$ processes are also related by isospin invariance through [47]:

$$\sigma_{pn\to d\pi^+\pi^-} = 2\sigma_{pn\to d\pi^0\pi^0} + \frac{1}{2}\sigma_{pp\to d\pi^+\pi^0}, \tag{4.13}$$

and

$$\sigma_{nn\to d\pi^-\pi^0} = \sigma_{pp\to d\pi^+\pi^0}. \tag{4.14}$$

For the processes described in eq. (4.13) the isospin breaking effects are strong, leading to a $\sim 25\%$ deviation [11]. Therefore the cross sections of these processes have been fitted individually by using the function [11]:

$$\sigma(\kappa) = \frac{a\kappa^b}{(c - \exp(d\kappa))^2 + e}, \tag{4.15}$$

for the $pp \to d\pi^+\pi^0$ and $pn \to d\pi^0\pi^0$ processes. The $pn \to d\pi^+\pi^-$ is described by [11]:

$$\sigma(\kappa) = \frac{a_1\kappa^{b_1}}{(c_1 - \exp(d_1\kappa))^2 + e_1} + \frac{a_2\kappa^{b_2}}{(c_2 - \exp(d_2\kappa))^2 + e_2}. \tag{4.16}$$

Here again $\kappa = k/(1\text{ GeV})$. The best fit parameters are shown in table 4.4.

$pn \to d\pi^0\pi^0$		$pn \to d\pi^+\pi^-$				$pp \to d\pi^+\pi^0$	
Parameter	Value	Parameter	Value	Parameter	Value	Parameter	Value
$a[\mu b]$	$2.855\ 10^6$	$a_1[\mu b]$	$6.465\ 10^6$	$a_2[\mu b]$	$2.549\ 10^{15}$	$a[\mu b]$	$5.099\ 10^{15}$
b	$1.311\ 10^1$	b_1	$1.051\ 10^1$	b_2	$1.657\ 10^1$	b	$1.656\ 10^1$
c	$2.961\ 10^3$	c_1	$1.979\ 10^3$	c_2	$2.330\ 10^7$	c	$2.333\ 10^7$
d	$5.572\ 10^0$	d_1	$5.363\ 10^0$	d_2	$1.119\ 10^1$	d	$1.133\ 10^1$
e	$1.461\ 10^6$	e_1	$6.045\ 10^5$	e_2	$2.868\ 10^{16}$	e	$2.868\ 10^{16}$

Table 4.4: Best fit values for the parameters of all $2 \to 3$ processes [11].

4.3 Kinematics

To take into account the recoil of the photon or the pion in any of the $2 \to 2$ processes, the following algorithm is applied in this thesis after the deuteron is created. The deuteron in the excited state gets boosted to the centre of mass frame. The new momentum of the deuteron and photon in the centre of mass frame is given by the conservation of energy and momentum:

$$\begin{bmatrix} E \\ \vec{0} \end{bmatrix} = \begin{bmatrix} E_1 \\ \vec{p} \end{bmatrix} + \begin{bmatrix} E_2 \\ -\vec{p} \end{bmatrix}. \tag{4.17}$$

By using the first equation the momentum can be determined from:

$$E = \sqrt{m_1^2 + p^2} + \sqrt{m_2^2 + p^2}. \tag{4.18}$$

With $m_1,\ m_2$ are the masses of the final state particles. Rearranging the terms in this equation gives the momentum in the centre of mass frame as:

$$p^2 = \frac{[E^2 - (m_1^2 + m_2^2)]^2 - 4m_1^2 m_2^2}{4E^2}. \tag{4.19}$$

After calculating the momentum of the final state deuteron, the direction is drawn uniformly from a sphere.

The processes with three particles as final states are more complicated. Corrections from matrix elements are neglected as there is not enough data available to perform any fits for the final deuteron CoM momentum distribution [11]. The momentum of the deuteron is therefore drawn randomly in the CoM frame from the kinematically allowed region. The differential decay rate for such a process is given by [49]:

$$d\Gamma = \frac{1}{(2\pi)^3} \frac{1}{32M^3} \overline{|\mathcal{M}|^2} dm_{12}^2 dm_{23}^2. \tag{4.20}$$

For our case the final state invariant masses are $m_{12} = m_{\pi\pi}$ and $m_{23} = m_{d\pi}$. Since the matrix element is assumed to be flat [11] the decay becomes a uniform distribution in the squares of the invariant masses. First it is necessary to determine the invariant mass of the two pions, which can be drawn from a uniform distribution in the region [49]:

$$\begin{aligned} m_{12,min}^2 &= (m_1 + m_2)^2, \\ m_{12,max}^2 &= (E - m_3)^2. \end{aligned} \tag{4.21}$$

In this process E is the energy of the decaying particle in the CoM frame as this process is treated as a $1 \rightarrow 3$ decay. With the invariant mass of the pions it is possible to determine the following quantities [49]:

$$\begin{aligned} E_2^* &= \frac{m_{12}^2 - m_1^2 + m_2^2}{2m_{12}}, \\ E_3^* &= \frac{E^2 - m_{12}^2 - m_3^2}{2m_{12}}, \end{aligned} \tag{4.22}$$

which are needed to draw the invariant mass m_{23} from a uniform distribution in the allowed range [49]:

$$\begin{aligned} m_{23,min}^2 &= (E_2^* + E_3^*)^2 - \left(\sqrt{E_2^{*2} - m_2^2} + \sqrt{E_2^{*3} - m_3^2}\right)^2 \\ m_{23,max}^2 &= (E_2^* + E_3^*)^2 - \left(\sqrt{E_2^{*2} - m_2^2} - \sqrt{E_2^{*3} - m_3^2}\right)^2. \end{aligned} \tag{4.23}$$

Then as a last step the deuteron momentum in the CoM frame is given by [11]:

$$p_d^2 = \frac{(s + m_d^2 - m_{d\pi}^2)^2}{4s} - m_d^2, \tag{4.24}$$

and as before the direction is drawn from a two-dimensional spherical uniform distribution.

4.4 Event Simulation

To simulate deuteron formation, the first step is to produce data for the protons and neutrons. This was done by using the latest version of the `Pythia` Monte Carlo (MC) event generator which is `Pythia 8240` [50, 51]. To reproduce the minimum bias events from the experiments, two incoming proton beams were used with the setting ‘‘`SoftQCD:nonDiffractive = on`’’. The maximum lifetime of the particles was defined by ‘‘`ParticleDecays:tau0Max = 1.0e-10`’’. To get the vertex information about the positions and times the particles were created the settings ‘‘`Fragmentation:setVertices = on`’’ is used. This is needed in the space-time model described in chapter 7. The centre of mass energies used were 0.9 TeV, 2.76 TeV and 7 TeV. After filtering out all events which have a proton and a neutron which could possibly produce a deuteron in the correct rapidity range [24] the following algorithms were used to simulate the deuteron formation. The codes used for anti-deuteron formation can be found in the github repository at https://github.com/RaphaelWag/deuteron_formation.

4.4.1 Coalescence Model

1. Find all events that contain at least one proton and one neutron.
2. In each event loop through all possible pairs of protons and neutrons:
   (a) Check each pair if the condition from eq. (4.1) is satisfied.
   (b) If the pair form a deuteron calculate the 4-momentum with eq. (4.19).
   (c) Exclude nucleus from future interactions if they formed a deuteron.

For the production of anti-deuterons the implementation is exactly the same just with the respective antiparticles as input. However, this method leads to potential systematical errors. The problem occurs in cases where there is in an event with multiple protons and/or neutrons. The order in which the protons and neutrons are combined might effect the deuteron distribution if there are multiple choices for successful (anti-)deuterons. However,we have checked that this error is negligible since forming a single deuteron is an extremely rare event.

4.4.2 Cross-Section Model

To produce deuterons with the cross section model the following algorithm is used:

1. Find all events that contain proton–neutron, proton–proton and neutron–neutron pairs.
2. Loop over all proton–neutron, proton–proton and neutron–neutron pairs in each event:
   (a) Save the probability for each pair.
   (b) Draw a random number r_i from a uniform distribution between 0 and 1 for each pair.
   (c) Select all pairs for which $r_i < P(X_1, X_2 \to dX_i|k)$ is satisfied.

(d) Repeat the following two steps until no selected pair is left:

i. From all selected pairs choose randomly one process. The probability to get chosen is given by the ratio of the individual probability compared to the sum of total probabilities of all selected processes that are left. Then create the corresponding deuteron.

ii. Exclude nuclei from further interactions.

Chapter 5

Re-weighting the Input Spectra

5.1 Input Proton Spectra

An interesting thing to investigate in models for anti-deuteron formation is the impact of the input spectra of the anti-protons and anti-neutrons. If a model gets an input which is inconsistent with the measurements it should produce wrong results. Therefore the first modification to the approach described above is to re-weight the spectra of the input nuclei. Figures 5.1 and 5.2 show the spectra for anti-protons measured at ALICE [31, 52] with a minimum bias trigger and V0AND mode as described in section 3.1, compared to the anti-proton spectra produced by `PYTHIA 8240` using the settings described in section 4.4. In figure 5.2 the proton and anti-proton spectra are divided in multiplicity classes as described in chapter 6. The spectra for 0.9, 2.76 and 7 TeV are normalized to NSD events while the 13 TeV spectra are normalized to INEL>0 events.

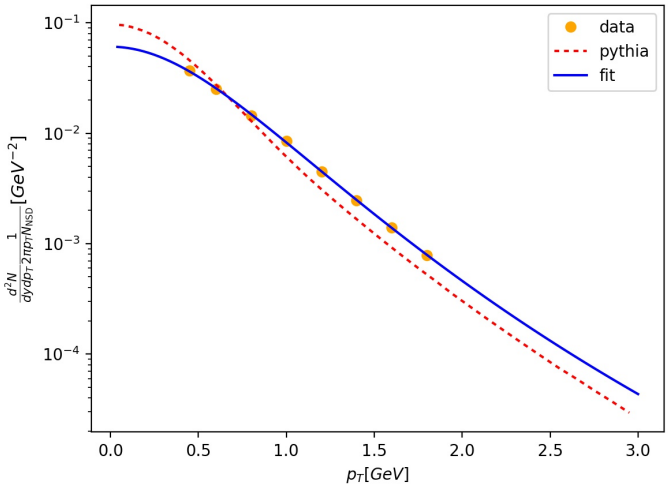

(a) 0.9 TeV

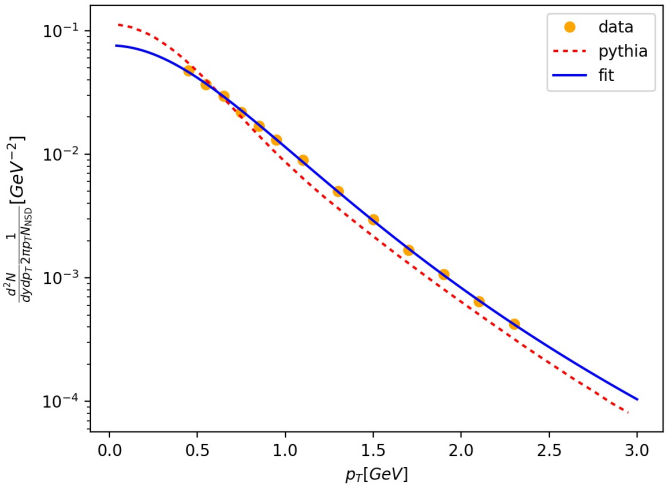

(b) 2.76 TeV

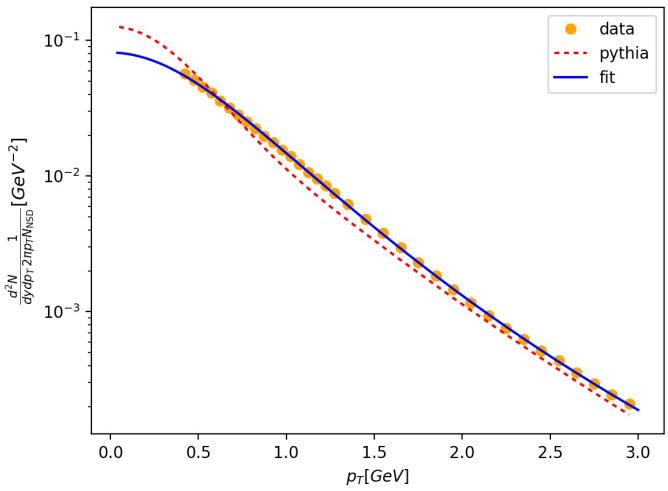

(c) 7 TeV

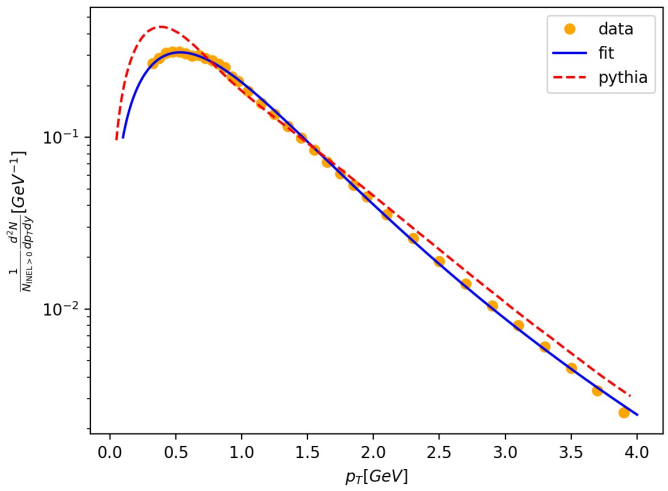

(d) 13 TeV

Figure 5.1: Transverse momentum spectra for anti-protons from ALICE [31], and combined spectra for anti-protons and protons [52] (data points), with their individual Levy-Tsallis fits eq. (3.12) (solid line) and the `PYTHIA` simulations (dashed line).

.

For 0.9 TeV and 7 TeV also other measurements [53, 54] could have been used, however for consistency reasons the measurements from [31] have been used.

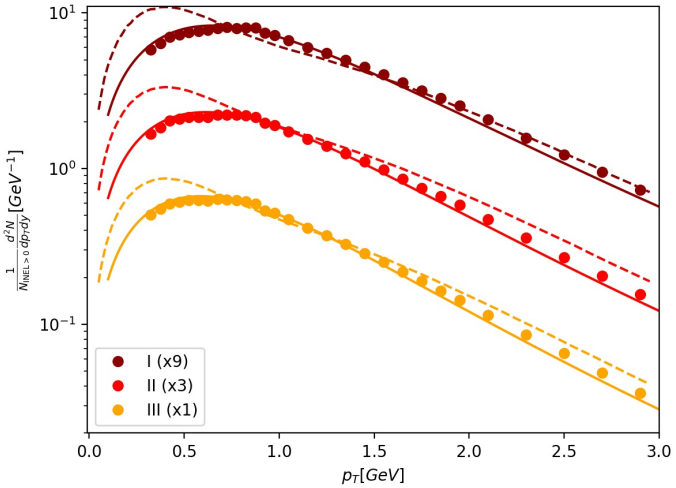

(a) 13 TeV

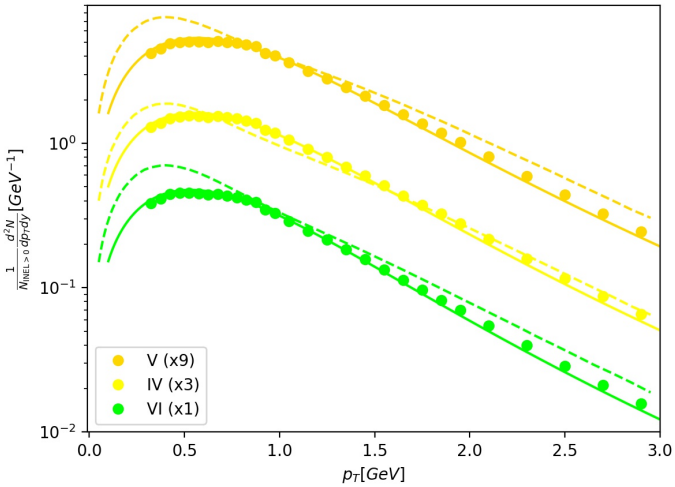

(b) 13 TeV

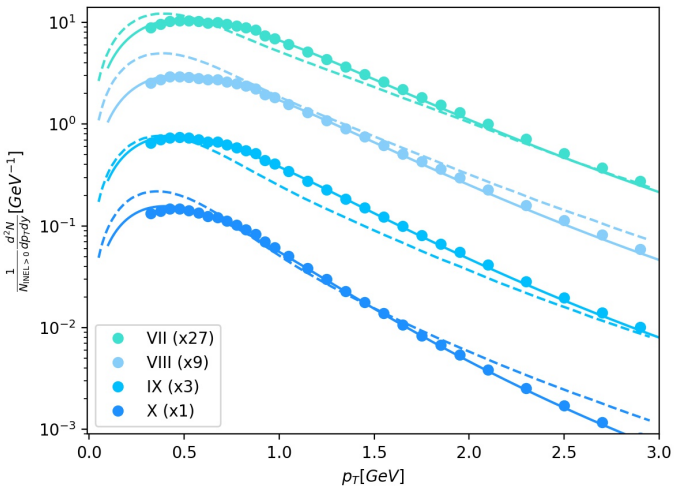

(c) 13 TeV

Figure 5.2: Multiplicity dependent transverse momentum spectra for protons and anti-protons from ALICE [52] (data points), with their individual Levy-Tsallis fits eq. (3.12) (solid line) and the `PYTHIA` simulations (dashed line).

.

The measured spectra has been fitted to the Levy-Tsallis distribution from eq. (3.12) to extrapolate the spectra for the low and high transverse momenta region, in order to be able to obtain weights outside the measured region. The values for the free fit parameters are shown in table 5.1. Unfortunately no χ^2 could be calculated

because the data sets for the proton spectra do not have error bars.

CoM Energy	$\frac{dN}{dy}$	n	C [GeV]
0.9 TeV	0.0992±0.0012	8.44±0.82	0.1922±0.0061
2.76 TeV	0.1352±0.0013	6.82±0.35	0.1985±0.0049
7 TeV	0.1684±0.0007	6.64±0.11	0.2224±0.0021
13 TeV	0.3691±0.0026	7.23±0.16	0.2442±0.0032

Table 5.1: Best-fit values for the free parameters of the Levy-Tsallis distribution from eq. (3.12), for the anti-proton spectra from [31] for 0.9, 2.76, 7 TeV and proton and anti-proton spectra from [52] for 13 TeV.

V0M	$\frac{dN}{dy}$	n	C [GeV]
I	1.358±0.035	8.62±0.29	0.3454±0.0090
II	1.061±0.026	8.35±0.25	0.3146±0.0078
III	0.871±0.019	8.01±0.18	0.2900±0.0060
V	0.750±0.016	7.84±0.15	0.2732±0.0052
IV	0.660±0.013	7.70±0.14	0.2600±0.0048
VI	0.555±0.012	7.49±0.14	0.2428±0.0048
VII	0.443±0.010	7.36±0.13	0.2239±0.0045
VIII	0.3539±0.0079	7.17±0.11	0.2054±0.0039
IX	0.2484±0.0041	7.016±0.065	0.1837±0.0024
X	0.1296±0.0036	6.81±0.10	0.1437±0.0031

Table 5.2: Best-fit values for the free parameters of the Levy-Tsallis distribution from eq. (3.12), for the multiplicity dependent proton and anti-proton spectra from ALICE at 13 TeV [52]

We can see in figure 5.1 that for 0.9, 2.76 and 7 TeV there is a consistent behaviour. For low transverse momenta the MC generator produces too many anti-protons while for higher transverse momenta there are too few anti-protons compared

to the experiments. This would lead to too many anti-deuterons produced in the low region and too many in the high transverse momenta region by the coalescence models. For 13 TeV there are mostly too many (anti-)protons in the multiplicity combined spectra and for all multiplicity classes except IX.

5.2 Re-weighting the Input Spectra

In order to compensate for the difference between the measurements and the MC event generator every proton and neutron gets a weight depending on their transverse momentum. The weights are given by the ratio of the number of protons from the data extended by the Levy-Tsallis fit compared to the number of protons produced by the MC event generator:

$$w(p_T) = \frac{N_{data}(p_T)}{N_{MC}(p_T)}. \tag{5.1}$$

For neutrons there is unfortunately no data available because the particle identification detectors only work on charged particles, therefore the weights for neutrons are assumed to be the same as for the protons. This is a reasonable approximation based on the isospin invariance of the strong force.

The deuterons produced in the coalescence models are then re-weighted by the product of the weights from their constituent proton and neutron:

$$w_d = w_p w_n. \tag{5.2}$$

Thus, instead of adding one deuteron to the histogram, there are w_d deuterons added to the histogram.

5.3 Results

Figure 5.3 shows the resulting χ^2 as a function of the free parameter, each of the coalescence models has. The χ^2 is given by:

$$\chi^2 = \frac{1}{N-\nu} \sum_{i=0}^{N} \frac{(N_{data,i} - N_{MC,i})^2}{\sigma_i^2}. \tag{5.3}$$

Here N is the number of degrees of freedom which is given by the number of bins of the histogram and ν is the number of free parameters, which is one for both models.

The weights for 13 TeV used in this chapter are determined by the spectra shown in figure 5.1d, and independent of multiplicity. The results show that in general it is possible to get very good individual fits for all used data sets by using weights. Only the cross-section model gives a slightly worse fit for the 13 TeV data compared to the other results. Without using weights the standard coalescence model is not able to reproduce any of the measurements. The cross-section model gives a much better fit without re-weighting the input spectra. However, the performance of both models increase drastically by using weights.

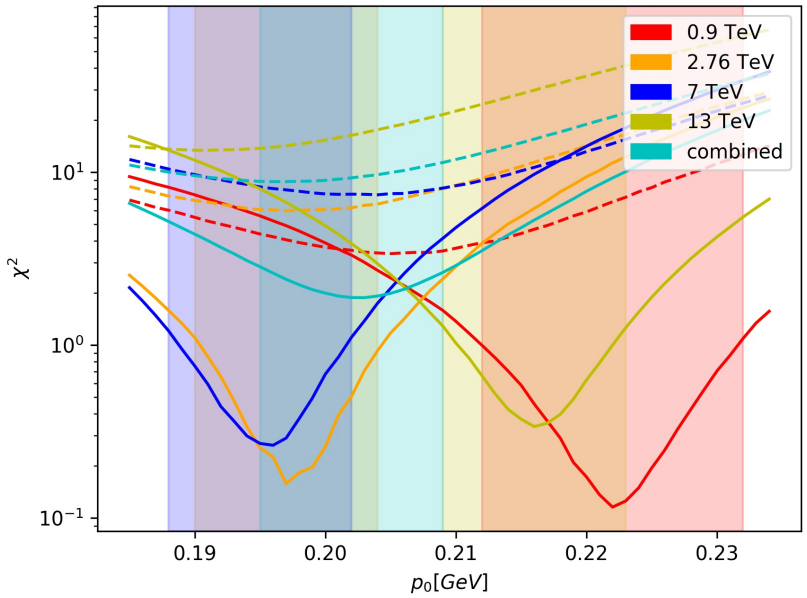

(a) Standard Coalescence Model

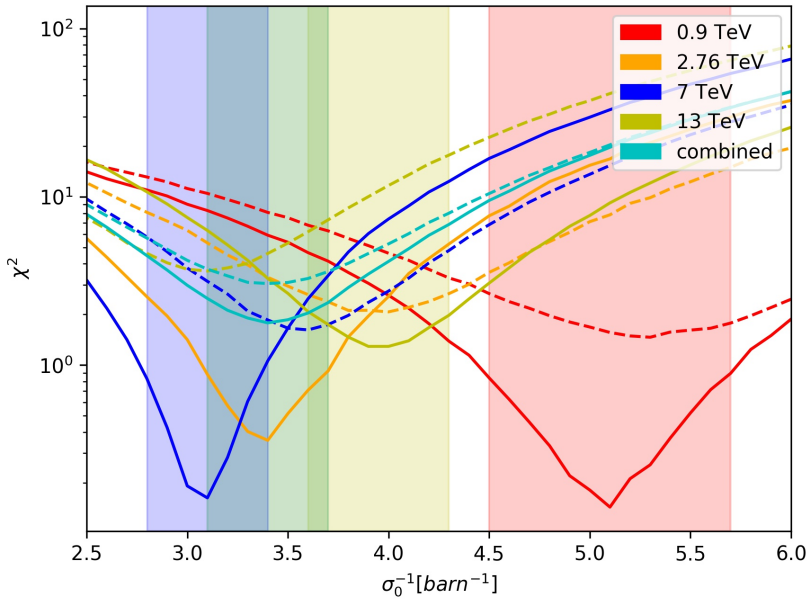

(b) Cross Section Model

Figure 5.3: χ^2 as a function of the free parameter of the coalescence models. The dashed lines are without using weights, the continuous lines are with weights. The coloured regions show the error in a 1σ range.

The best fit values and the corresponding χ^2 values for both models are shown

in table 5.3.

CoM Energy	p_0[MeV]	χ^2	σ_0^{-1}[barn^{-1}]	χ^2
0.9 TeV	205^{+9}_{-9}	3.38	$5.3^{+0.7}_{-0.7}$	1.46
2.76 TeV	197^{+8}_{-7}	5.98	$4.0^{+0.4}_{-0.5}$	2.07
7 TeV	204^{+6}_{-9}	7.40	$3.6^{+0.3}_{-0.3}$	1.62
13 TeV	191^{+6}_{-6}	13.40	$3.1^{+0.3}_{-0.3}$	3.62
combined	196^{+8}_{-7}	8.82	$3.4^{+0.4}_{-0.3}$	3.05

(a) Without re-weighting the input spectra.

CoM Energy	p_0[MeV]	χ^2	σ_0^{-1}[barn^{-1}]	χ^2
0.9 TeV	222^{+10}_{-10}	0.12	$5.1^{+0.6}_{-0.6}$	0.14
2.76 TeV	197^{+7}_{-7}	0.16	$3.4^{+0.3}_{-0.3}$	0.36
7 TeV	196^{+6}_{-8}	0.26	$3.1^{+0.3}_{-0.3}$	0.16
13 TeV	216^{+7}_{-7}	0.34	$3.9^{+0.4}_{-0.3}$	1.29
combined	203^{+6}_{-8}	1.88	$3.4^{+0.3}_{-0.3}$	1.78

(b) With re-weighting the input spectra.

Table 5.3: Best fit values and corresponding χ^2 for the coalescence models.

Here the results clearly show that without using weights the standard coalescence model can not produce a satisfying fit for any of the data sets. The cross section model gives a much better fit without using weights but still has high χ^2 values. By using weights the fits improve drastically and reproduce the measured spectra very well. The spectra differential in event multiplicity are discussed in chapter 6.

Figure 5.4 shows the spectra produced by the best fit values for the standard coalescence model.

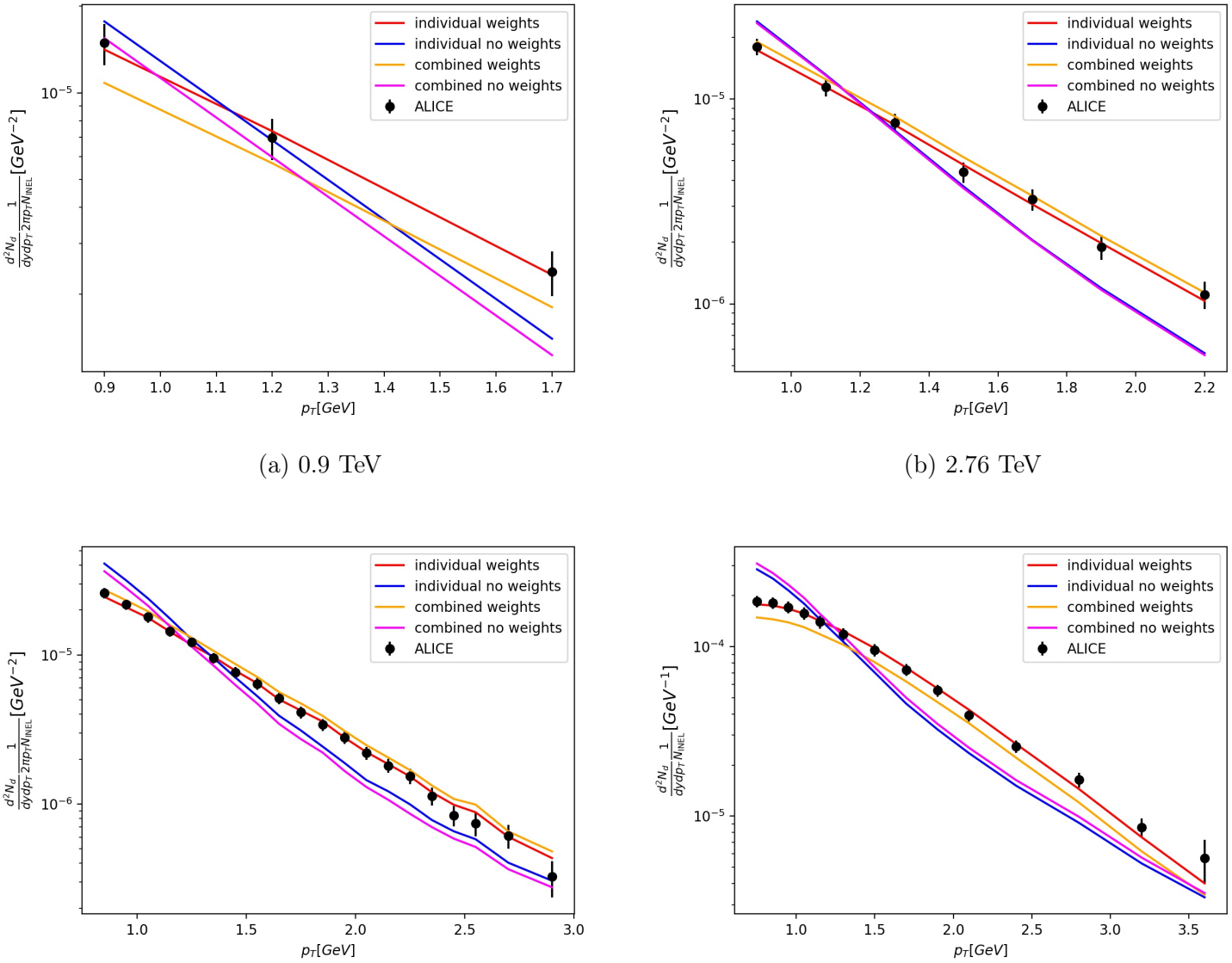

(a) 0.9 TeV

(b) 2.76 TeV

(c) 7 TeV

(d) 13 TeV

Figure 5.4: Transverse momentum spectra for anti-deuterons from the ALICE [24, 26] experiment (data points) compared to the spectra produced by the standard coalescence model with the best fit parameters with and without weights.

These figures show the resulting anti-deuteron spectra using the anti-proton spectra shown in figure 5.1. The slope of the unweighted spectra does not fit the measurements as there are too many anti-deuterons in the low and too few in the high transverse momentum region. This behaviour can be seen in all data-sets.

By using weights this problem is corrected and the fits look very similar to the measurements, with the exception of the combined fit with weights which does not reproduce the spectra for 0.9 TeV.

Figure 5.5 shows the spectra produced with the best fit values using the cross-section model.

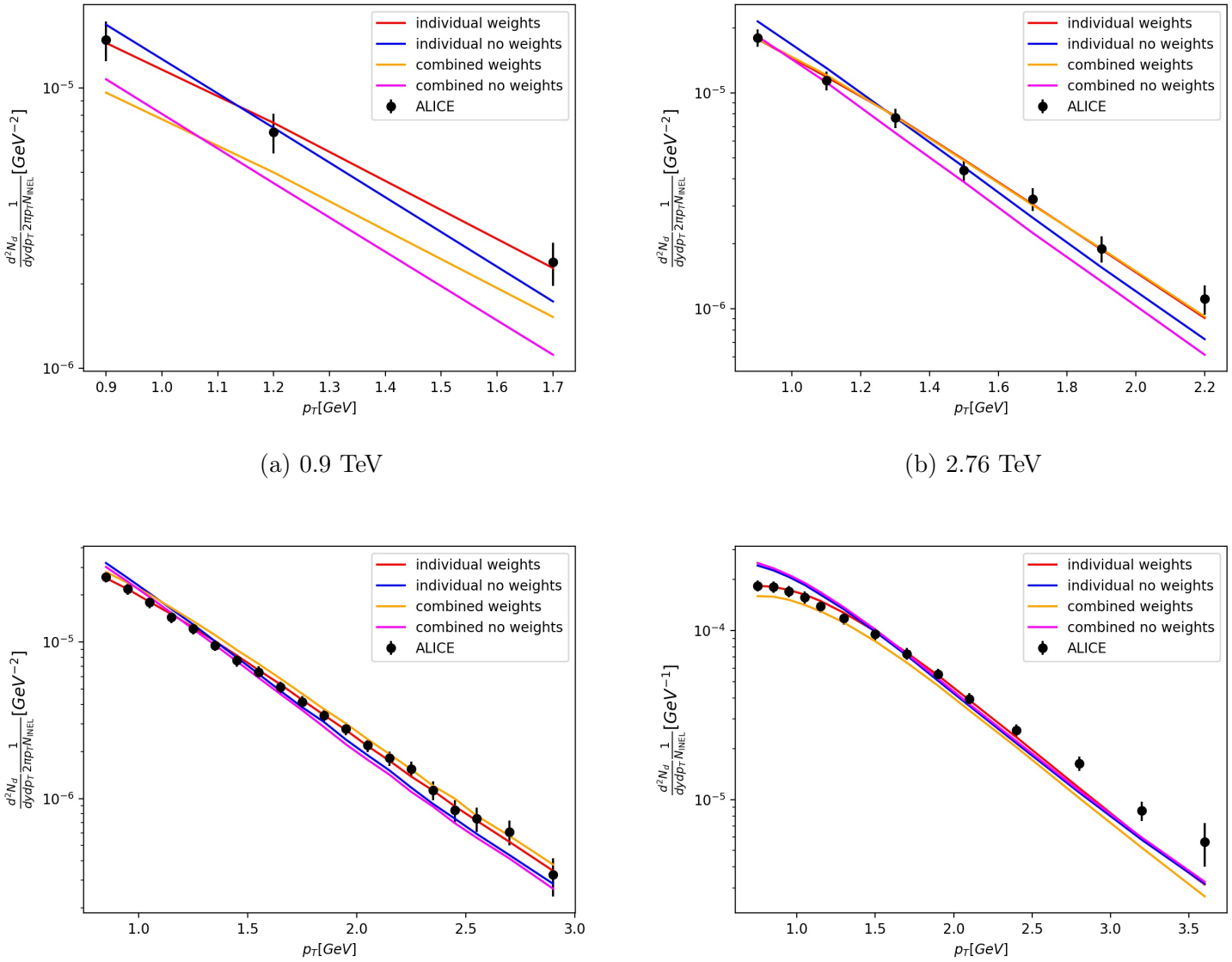

(a) 0.9 TeV

(b) 2.76 TeV

(c) 7 TeV

(d) 13 TeV

Figure 5.5: Transverse momentum spectra for anti-deuterons from the ALICE [24] experiment (data points) compared to the spectra produced by the cross section model with the best fit parameters with and without weights.

As already discussed above the figure shows that the cross section model gives a much better fit than the standard coalescence model without using weights. However, the main problem is still the same. The slope of the unweighted spectra has too many anti-deuterons in the low transverse momentum region and too few in

the high region. By using weights the fit of the simulated spectra improves very well except for the high transverse momenta region for 13 TeV, as there are too few anti-deuterons, and as for the standard coalescence model before, the combined fit produces too few anti-deuterons for the 0.9 TeV data.

Chapter 6

Multiplicity Dependence

Recently published measurements of (anti-)deuteron spectra from ALICE [25, 26] are presented in different event multiplicity classes. This gives more insight in the processes and allows to study the formation models in more detail. In high multiplicity classes anti-deuteron production could not only come from coalescence. There might be a significant contribution to the spectra coming from direct hadronization in the fireball. Therefore there might be a higher p_0, σ_0^{-1} parameter for higher event multiplicity

6.1 Definition of Multiplicity Classes

The measurements of anti-deuterons used in this chapter are divided into event classes based on the total ionisation energy deposited in the forward and backward detector regions. This is called the "V0M" (VZERO Multiplicity) amplitude. The V0M amplitude is linearly proportional to the number of primary charged particles [55] produced in the V0 detectors acceptance. These detectors are the V0A and V0C detectors which cover the pseudo-rapidity regions of $2.8 < \eta < 5.1$ and $-3.7 < \eta < -1.7$, respectively. The classes are indicated by roman numerals and defined in fractions of the total INEL>0 cross-section with increasing charged particle multiplicity.

The definition of the classes is shown in tables 6.1 and 6.2.

Class	I	II	III	IV	V
$\sigma/\sigma_{\mathrm{INEL>0}}$	0–0.92%	0.92–4.6%	4.6–9.2%	9.2–13.8%	13.8–18.4%
Class	VI	VII	VIII	IX	X
$\sigma/\sigma_{\mathrm{INEL>0}}$	18.4–27.6%	27.6–36.8%	36.8–46.0%	46.0–64.5%	64.5–100%

Table 6.1: Event multiplicity classes and their corresponding fraction of the INEL>0 cross-section ($\sigma/\sigma_{\mathrm{INEL>0}}$) used in [52]. The lowest roman numeral corresponds to the highest multiplicity class.

Class	I	II	III	IV	V
$\sigma/\sigma_{\mathrm{INEL>0}}$	0–0.95%	0.95–4.7%	4.7–9.5%	9.5–14%	14–19%
Class	VI	VII	VIII	IX	X
$\sigma/\sigma_{\mathrm{INEL>0}}$	19–28%	28–38%	38–48%	48–68%	68–100%

Table 6.2: Event multiplicity classes and their corresponding fraction of the INEL>0 cross-section ($\sigma/\sigma_{\mathrm{INEL>0}}$) used in [56]. The lowest roman numeral corresponds to the highest multiplicity class.

In previous measurements the event classification was based on the charged particle densities in the mid pseudo-rapidity region [57], while here the forward and backward pseudo-rapidity region is used. This choice is due to the fact that performing multiplicity selection and measurements in overlapping regions can lead to auto-correlation biases and unphysical results [58]. In [59] the multiplicity dependence of (multi-)strange hadron production in proton–proton collisions at $\sqrt{s} = 13$ TeV was studied. The analysis is performed with three different multiplicity estimators. The used estimators are the V0M amplitude as described above, and the number of charged tracklets in two pseudo-rapidity regions: $|\eta| < 0.8$ and $0.8 < |\eta| < 1.5$. The results of their analysis shows that using the multiplicity estimators which are disjoint from the region of the data analysis (V0M and the outer tracklets) show a similar behaviour, while the estimator overlapping with the region of the data

analysis shows a systematically different behaviour.

For the measurements of (anti-) deuterons at 7 and 13 TeV [25, 26] investigated here only the V0M estimator is used. Figure 6.1 shows our simulation of the distribution of charged particles per unit pseudo rapidity produced by `PYTHIA 8` at 13 TeV for the three multiplicity estimators used in [59] and with the class definition from table 6.2. The settings in `PYTIHA 8` used to obtain these distributions were not the same as described in section 4.4. For the anti-deuteron production only ND events contribute to the spectra. However, for these distributions all INEL>0 events must be taken into account. Therefore the settings are changed from producing ND events to produce all INEL events. Then all events with charged particles in both V0 detectors and the mid region $|\eta| < 1$ are used.

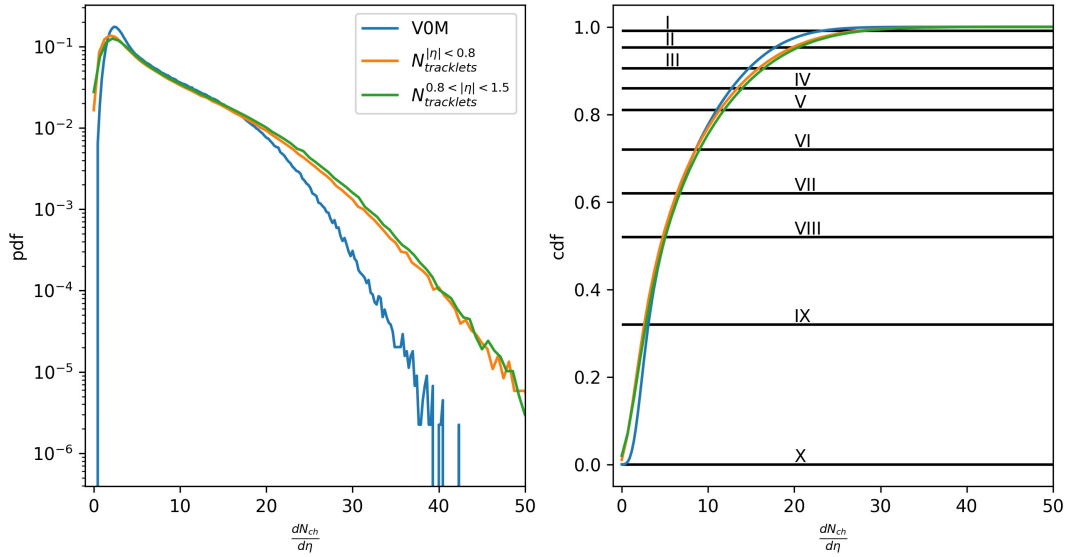

Figure 6.1: Probability distribution of charged particles per unit η simulated by `PYTHIA 8`.

The plot shows that the distribution in the mid region is significantly different than the distribution in the V0 detectors as there are in general less charged particles in the forward and backward regions. We use the charged particle distribution for V0M presented in figure 6.1 to determine the multiplicity class of an event. Since (anti-) deuterons are measured at mid rapidity $|y| < 0.5$, the production of these

anti-deuterons could get influenced by the charged particle distribution in the mid region. Table 6.3 and 6.4 compares the average number of charged particles per unit pseudo-rapidity in the mid region $|\eta| < 0.5$ from the ALICE measurements [52, 56, 59] and our PYTHIA simulations.

	7 TeV V0M		13 TeV V0M	
Class	ALICE	PYTHIA	ALICE	PYTHIA
I	21.3±0.6	19.97±0.24	26.02±0.35	24.60±0.22
II	16.5±0.5	16.36±0.11	20.02±0.27	19.84±0.09
III	13.5±0.4	13.60±0.08	16.17±0.22	16.43±0.09
IV	11.5±0.3	11.74±0.13	13.77±0.19	14.14±0.08
V	10.1±0.3	10.24±0.07	12.04±0.17	12.38±0.09
VI	8.45±0.25	8.49±0.05	10.02±0.14	10.11±0.05
VII	6.72±0.21	6.78±0.05	7.95±0.11	7.94±0.04
VIII	5.40±0.17	5.10±0.02	6.32±0.09	6.25±0.02
IX	3.90±0.14	3.40±0.02	4.50±0.07	4.19±0.03
X	2.26±0.12	2.38±0.01	2.55±0.04	2.51±0.01
INEL>0	5.96±0.23	5.90±0.02	6.89±0.11	6.89±0.02

Table 6.3: $\langle dN_{ch}/d\eta \rangle_{|\eta|<0.5}$ for 7 and 13 TeV from ALICE [52, 56] and PYTHIA. For 7 TeV the event class definitions from table 6.2 are used, while for 13 TeV the definitions from table 6.1 are used.

In order to study in more detail how well PYTHIA reproduces the charged particle distributions compared to the measurements, table 6.4 shows the average number of charged particles measured in [59] compared to the simulations.

	ALICE			PYTHIA		
Class	V0M	$N^{\lvert\eta\rvert<0.8}_{\text{tracklets}}$	$N^{0.8<\lvert\eta\rvert<1.5}_{\text{tracklets}}$	V0M	$N^{\lvert\eta\rvert<0.8}_{\text{tracklets}}$	$N^{0.8<\lvert\eta\rvert<1.5}_{\text{tracklets}}$
I	25.75±0.40	32.49±0.50	26.32±0.40	24.60±0.22	31.15±0.28	25.79±0.20
II	19.83±0.30	23.42±0.35	19.51±0.29	19.84±0.09	22.71±0.07	20.07±0.08
III	16.12±0.24	18.29±0.28	15.45±0.23	16.43±0.09	17.83±0.04	16.33±0.13
IV	13.76±0.21	14.90±0.23	13.14±0.20	14.14±0.08	14.80±0.04	14.20±0.09
V	12.06±0.18	12.90±0.19	11.63±0.17	12.64±0.11	12.64±0.02	12.14±0.05
VI	10.11±0.15	10.72±0.16	9.50±0.14	10.18±0.05	10.08±0.03	9.95±0.05
VII	8.07±0.12	8.14±0.12	7.68±0.11	7.71±0.03	7.66±0.02	7.62±0.02
VIII	6.48±0.10	5.95±0.09	6.35±0.10	6.01±0.01	5.78±0.01	5.69±0.03
IX	4.64±0.07	3.82±0.06	4.36±0.06	3.93±0.03	3.88±0.01	3.97±0.03
X	2.52±0.04	1.76±0.03	2.67±0.04	2.45±0.01	1.86±0.01	2.45±0.01
INEL>0		6.89±0.11			6.89±0.02	

Table 6.4: $\langle dN_{ch}/d\eta \rangle_{|\eta|<0.5}$ for 13 TeV from ALICE [59] and PYTHIA. The definition of the event classes used here are given in table 6.2.

Overall PYTHIA reproduces the charged particle distribution well in all multiplicity classes even if it is not perfect. While in the lower and higher multiplicity classes the average number of charged particles is some what too small the mid multiplicity classes contain too many charged particles. This behaviour can be seen in the disjoint estimators V0M and outer tracklets, while there are in general too few charged particles in the inner tracklets.

6.2 Data Sets

The measurements of anti-deuterons used here are presented in [25, 26]. The used CoM energies are 7 TeV and 13 TeV. In both cases some multiplicity classes have been combined in the measurements to reduce the statistical error. The spectra are shown in figure 6.2 and 6.3 with out Levi-Tsallis fits. While for 7 TeV the event class definition in table 6.2 is used, for 13 TeV the definition in table 6.1 is used. For some data points the errors are too small to be visible.

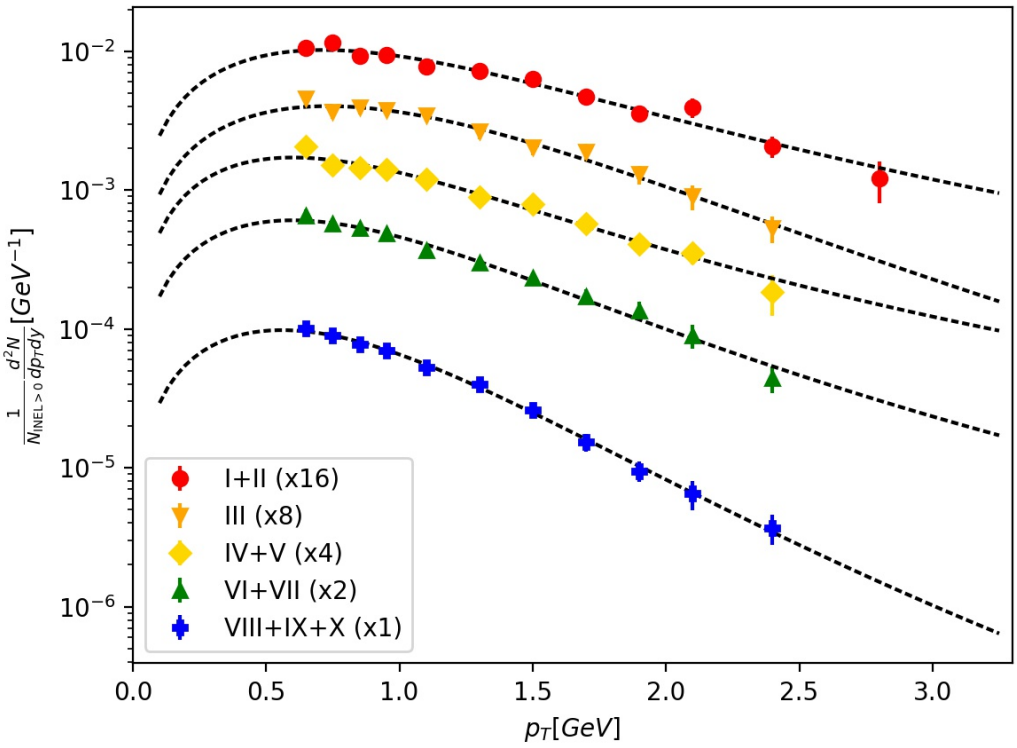

Figure 6.2: Transverse-momentum spectra of anti-deuterons measured in proton–proton collisions at $\sqrt{s} = 7$ TeV in different multiplicity classes [25] with their individual Levy-Tsallis fits (3.12).

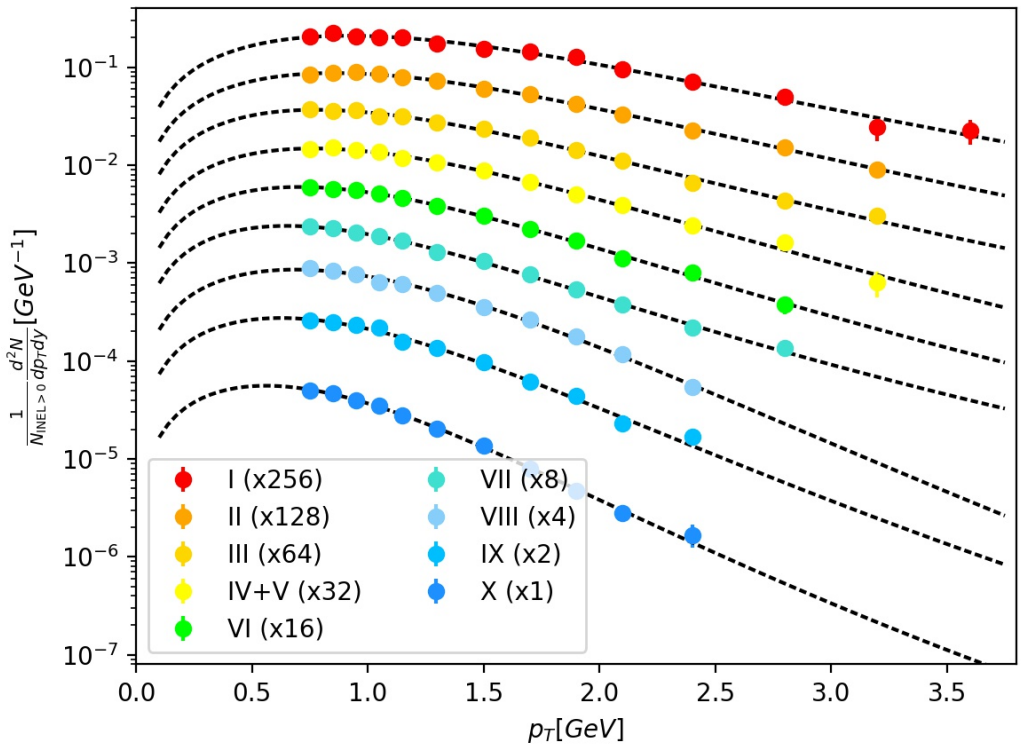

Figure 6.3: Transverse-momentum spectra of anti-deuterons measured in proton–proton collisions at $\sqrt{s} = 13$ TeV in different multiplicity classes [26] with their individual Levy-Tsallis fits (3.12).

The fitted solutions for the free fit parameters of the Levy-Tsallis distribution (3.12) are presented in table 6.5.

Class	$\frac{dN}{dy}[\times 10^{-4}]$	n	C [GeV]	χ^2
I+II	10.95±0.90	3.7±1.1	0.219±0.039	0.70
III	7.41±0.29	7.7±3.6	0.248±0.030	0.37
IV+V	6.23±0.59	3.3±0.9	0.155±0.034	0.68
VI+VII	3.89±0.18	4.6±1.0	0.162±0.022	0.54
VIII+IX+X	1.066±0.029	7.2±1.2	0.148±0.010	0.19

(a) 7 TeV

Class	$\frac{dN}{dy}[\times 10^{-4}]$	n	C [GeV]	χ^2
I	16.06±0.43	7.0±1.9	0.372±0.028	0.32
II	12.23±0.14	7.2±0.8	0.329±0.011	0.08
III	9.38±0.19	6.2±1.0	0.272±0.017	0.28
IV+V	7.11±0.12	8.2±1.4	0.271±0.013	0.21
VI	5.307±0.092	7.4±1.1	0.231±0.012	0.17
VII	3.987±0.071	6.1±0.7	0.195±0.010	0.15
VIII	2.732±0.066	17.9±7.9	0.229±0.015	0.32
IX	1.632±0.074	10.3±4.7	0.188±0.022	0.78
X	0.591±0.015	9.7±1.6	0.1519±0.0082	0.11

(b) 13 TeV

Table 6.5: Best fit values for the free parameters of the Levy-Tsallis distribution (3.12) for all used multiplicity classes for 7 TeV and 13 TeV.

6.3 Results

The standard coalescence model and cross-section model have been fitted to the anti-deuteron spectra deferential in multiplicity. The input spectra of anti-protons and anti-neutrons were generated by `PYTHIA` with the settings as described in section 4.4. The fits were done by using weights as described in section 5.2. For 13 TeV the weights are determined by the spectra in figure 5.2 and are therefore individual

for each multiplicity class. Figure 6.4 and 6.5 show the resulting χ^2 eq. (5.3) as a function of the free parameter, each of the coalescence models have for 7 TeV and 13 TeV.

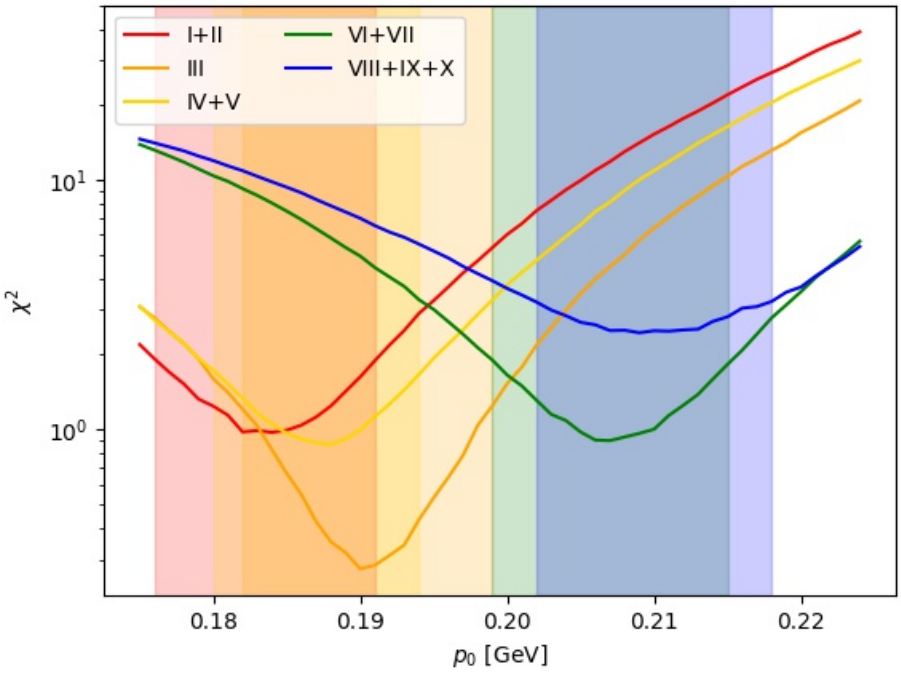

(a) Standard Coalescence Model

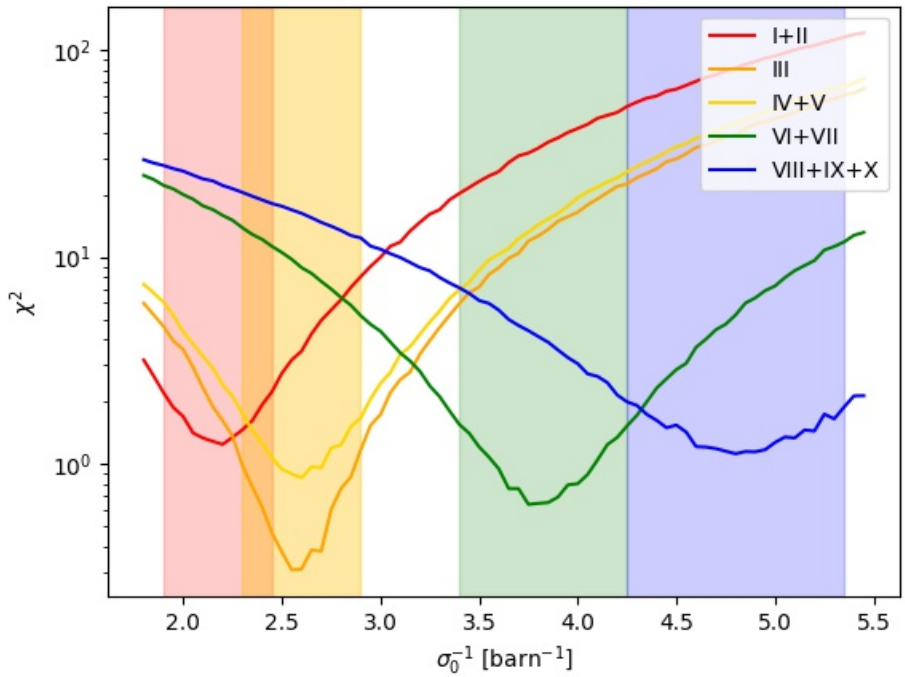

(b) Cross Section Model

Figure 6.4: χ^2 as a function of the free parameter p_0, σ_0 of the coalescence models for different multiplicity classes at 7 TeV. The coloured bands show the one sigma error range.

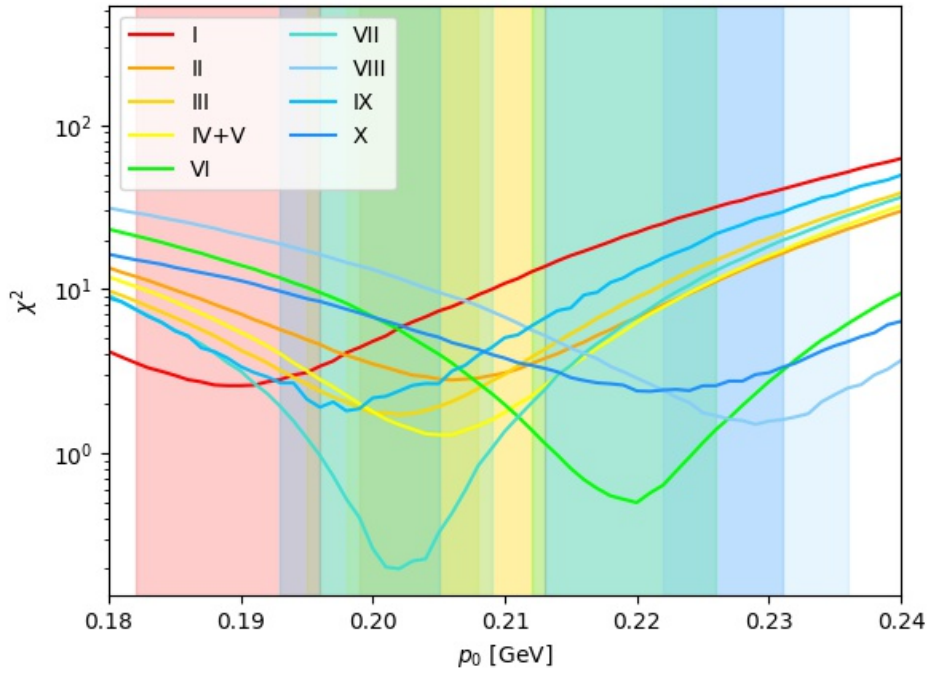

(a) Standard Coalescence Model

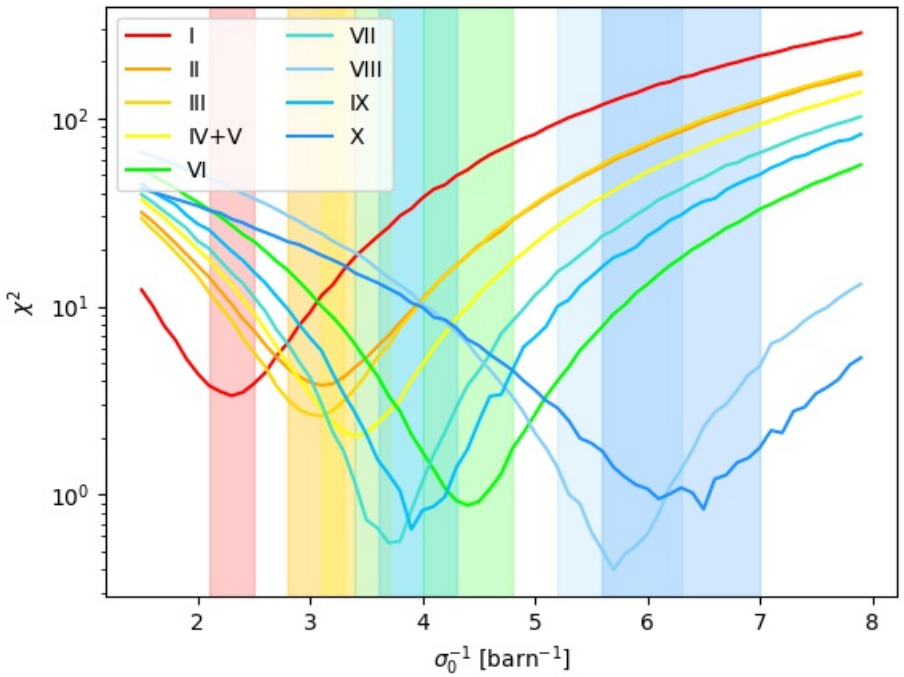

(b) Cross Section Model

Figure 6.5: χ^2 as a function of the free parameter p_0, σ_0 of the coalescence models for different multiplicity classes at 13 TeV. The coloured bands show the error in a 1σ range.

The best fit values and the corresponding χ^2 values for both models are shown in tables 6.6

V0M class	p_0[MeV]	χ^2	σ_0^{-1}[barn^{-1}]	χ^2
I+II	184^{+7}_{-8}	0.97	$2.20^{+0.25}_{-0.30}$	1.25
III	190^{+9}_{-8}	0.28	$2.55^{+0.35}_{-0.25}$	0.31
IV+V	188^{+6}_{-8}	0.87	$2.60^{+0.30}_{-0.30}$	0.86
VI+VII	207^{+8}_{-8}	0.90	$3.75^{+0.50}_{-0.35}$	0.64
VIII+IX+X	209^{+7}_{-7}	2.43	$4.80^{+0.55}_{-0.55}$	1.22

(a) 7 TeV

V0M class	p_0[MeV]	χ^2	σ_0^{-1}[barn^{-1}]	χ^2
I	190^{+6}_{-8}	2.58	$2.3^{+0.2}_{-0.2}$	3.35
II	206^{+7}_{-7}	2.80	$3.1^{+0.3}_{-0.3}$	3.80
III	202^{+6}_{-7}	1.71	$3.1^{+0.2}_{-0.3}$	2.62
IV+V	206^{+6}_{-8}	1.29	$3.4^{+0.3}_{-0.3}$	2.00
VI	220^{+6}_{-8}	0.50	$4.4^{+0.4}_{-0.4}$	0.88
VII	202^{+7}_{-6}	0.20	$3.7^{+0.3}_{-0.3}$	0.55
VIII	229^{+7}_{-7}	1.50	$5.7^{+0.5}_{-0.5}$	0.40
IX	198^{+7}_{-5}	1.81	$3.9^{+0.4}_{-0.3}$	0.65
X	221^{+10}_{-8}	2.38	$6.5^{+0.5}_{-0.9}$	0.83

(b) 13 TeV

Table 6.6: Best fit values and corresponding χ^2 for the coalescence models for the multiplicity dependent spectra.

We can see that for 7 TeV the models give in general good fits, except for the coalescence model in the lower multiplicity class VIII+IX+X. Both models show that for higher multiplicity there is a lower coalescence parameter which is against our prior assumption that we should expect a higher coalescence parameter in the MC simulation due to extra anti-deuteron production coming from direct hadronization in the fireball at the early stage of the collision.

For 13 TeV the standard coalescence model only gives good fits in the mid multiplicity classes IV-VIII. Also here the coalescence parameter shows a tending to increase with decreasing event multiplicity. However, it is not as clearly visible as for 7 TeV. The cross section model gives very good fits for 7 TeV with a clear separation between high and low multiplicity. However, for 13 TeV the cross section model gives good fits only for the low multiplicity spectra and becomes worse for high multiplicity. Also for 13 TeV the low multiplicity classes VI-X have a significant higher σ_0^{-1} values compared to high multiplicity classes I-V.

Figure 6.6 shows the best fits for both coalescence models for all multiplicity classes at 7 TeV and 13 TeV with their individual best fit parameter.

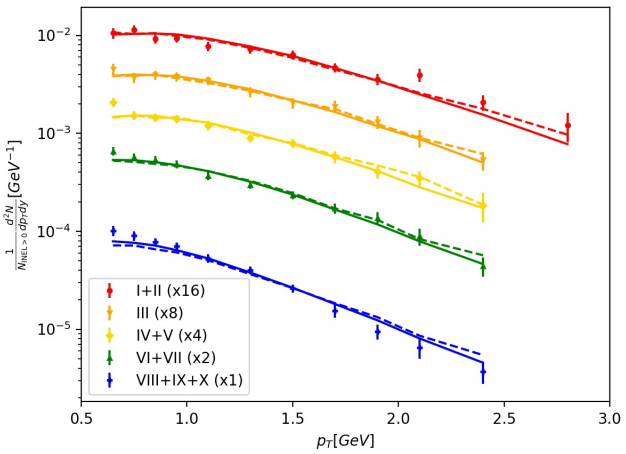

(a) 7 TeV

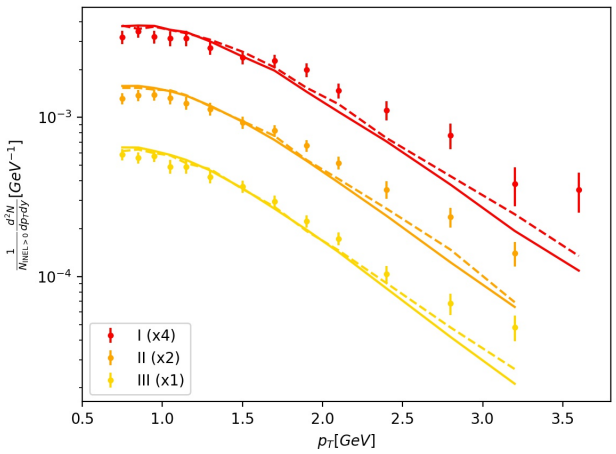

(b) 13 TeV

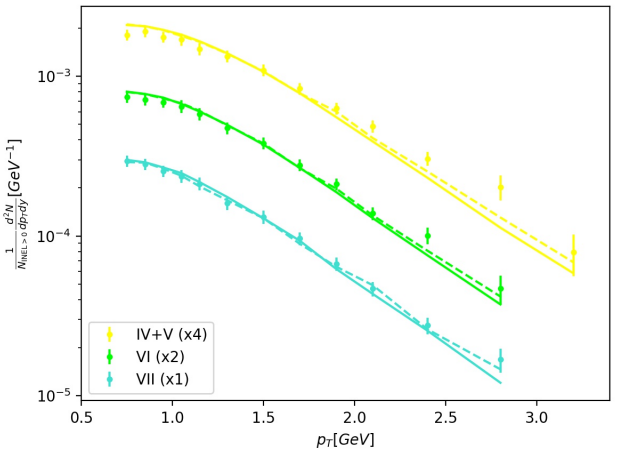

(c) 13 TeV

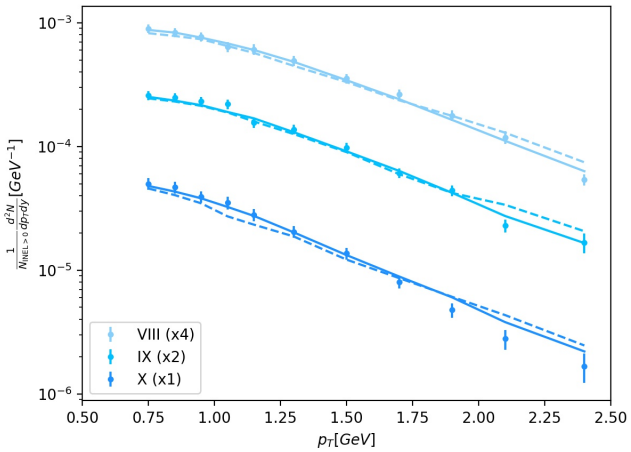

(d) 13 TeV

Figure 6.6: Anti-deuteron spectra produced by the standard coalescence model (dashed line) and cross-section model (solid line), compared to the measurements at ALICE [25, 26] (data points).

The results show that for the lowest multiplicity class at 7 TeV the shape of the spectra produced by the coalescence model does not fit the data points, which is not the case for the cross-section model. For 13 TeV the standard coalescence model gives a rather poor fit for the lowest and highest multiplicity classes. The cross section model gives good fits for the low multiplicity classes at 13 TeV with χ^2

values below 1. However, it becomes worse for high multiplicity, with χ^2 values above 2, as there are too few anti-deuterons at high p_T. This was already the case in the multiplicity independent fit shown in figure 5.5d. The spectra produced by the coalescence models both produce too few anti-deuterons for high multiplicity in the high transverse momenta range. This could be caused by the fact that the high-end tail of the multiplicity distribution in `PYTHIA` is different from the experiments. On the other hand the reason for the bad fits at high multiplicity could aswell be caused by the coalescence models being unable to describe anti-deuteron formation at high multiplicity.

As mentioned in the beginning of this chapter there might be a significant contribution to the anti-deuteron spectra from direct hadronization in the fireball. This would lead to a higher p_0, σ_0^{-1} value for high multiplicity. However, the results of table 6.6 show the coalescence parameters are decreasing instead of increasing. This is a very similar behaviour to the results of the studied B_2 coalescence parameter [1] in [26]. As discussed in [60] the coalescence parameter could depend on the source size which is in their model related to the event multiplicity. In this model higher event multiplicity corresponds to a bigger fireball, which is the source where the anti-deuterons are created. Since a bigger source means that the anti-neutron and anti-proton which could possibly form an anti-deuteron have a smaller wave function overlap, the coalescence parameter should decrease.

[1] The B_2 coalescence parameter is related to the p_0 parameter by: $B_2 = 2\left(\frac{4\pi}{3}\frac{p_0^3}{m_N}\right)$, where m_N is the nucleon mass

Chapter 7

Position–Momentum Modelling

The particles in event generators like PYTHIA are quantum mechanical objects and should be treated like that. However, since this would be very hard to do, the models used in event generators treat particles mostly in a classical way [61]. In quantum mechanics position and momentum are not independent and can not be determined at the same time. This is not the case in the classical approximations used in event generators, where every particle is given a sharp 4-vector for position and momentum. The aim here is to improve the standard coalescence model by taking into account the space-time positions as well as the momenta of the nuclei. In a quantum mechanical treatment this would mean taking into account the overlap of the wave-functions. Here, however, we must contend ourselves with the phenomenological models of the Monte Carlo generator.

7.1 Correlations in Monte Carlo Simulations

In order to make a model that uses both, the positions and the momenta of the produced nuclei, it is important to understand how the distribution of the positions and momenta looks like in different models. The spectra shown in this chapter are produced with the same setting in PYTHIA as described in section 4.4.

The model used in PYTHIA for calculating the space-time production vertices is described in [61]. In this string-fragmentation model the production vertices are calculated in energy–momentum space and then translated by a linear transformation into space–time, which is based on the linear relationship between distance and energy in the QCD potential at large distances. The QCD potential is given by $V_{QCD}(r) \approx -\frac{4}{3}\frac{\alpha_s}{r} + \kappa r$. Here α_s is the strong coupling constant and $\kappa \approx 1$ GeV/fm measured in hadron spectroscopy (Regge trajectories). For calculating the space-time production vertices only the linear term is used in the model implemented in PYTHIA.

Figure 7.1 shows scatter plots of the simulated differences in the positions and momenta of proton–neutron pairs in their CoM frame in minimum bias collisions. The strength of the colour represents the product of the weights of the anti-proton and anti-neutron as described in chapter 5. Figure 7.2 shows the weighted distribution of the position differences of anti-proton–anti-neutron pairs normalized to a probability distribution.

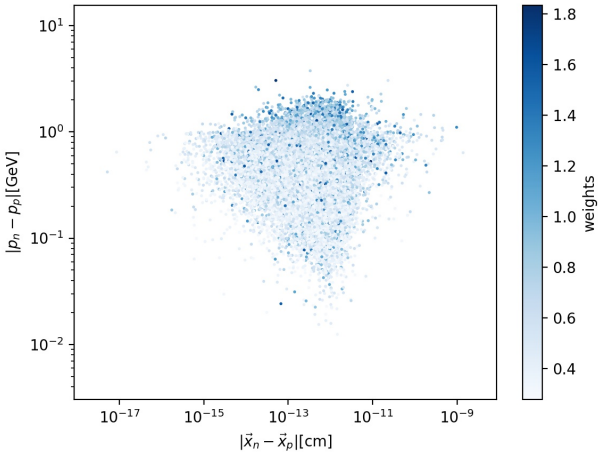

(a) 0.9 TeV

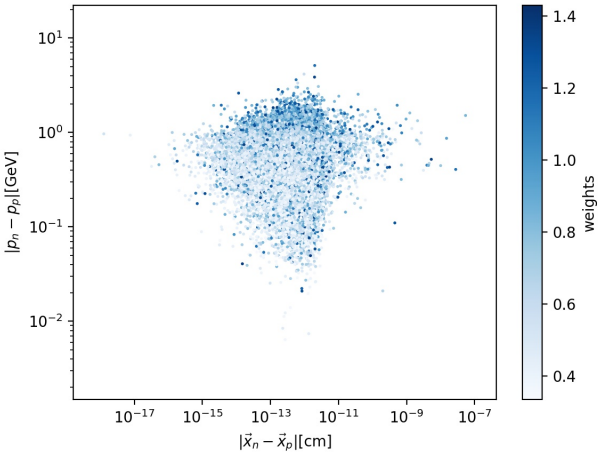

(b) 2.76 TeV

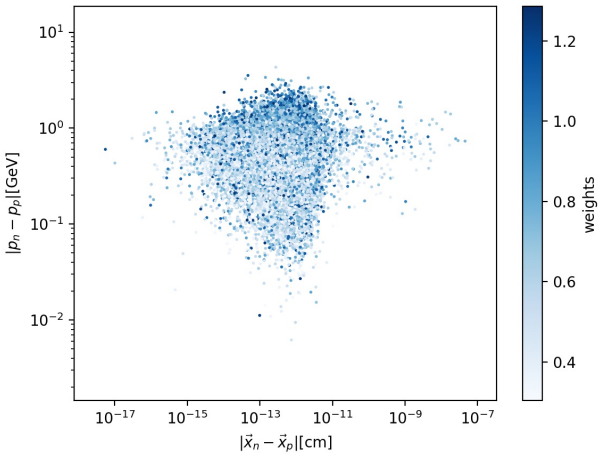

(c) 7 TeV

Figure 7.1: Scatter plots of position and momentum differences of proton–neutron pairs in `PYHTIA 8` minimum bias collisions.

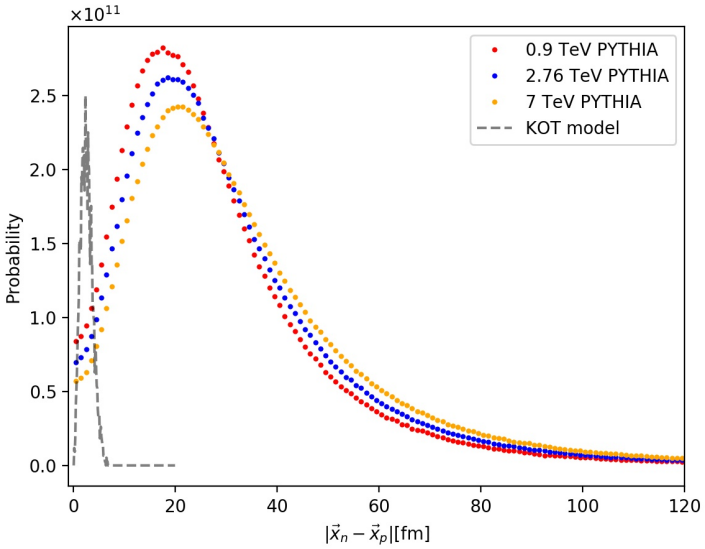

Figure 7.2: Probability distribution of position differences of proton–neutron pairs.

The plots show that for all used CoM energies the distributions have a similar structure. Most pairs are in a range of 10^{-15}cm to 10^{-10}cm which is comparable to the size of a nucleon which is 10^{-13}cm. Coalescence when the nuclei are 10^{-10}cm apart would be unrealistic because the wave functions do not overlap at such big distances. Also the mean value of $\langle|\vec{x}_n - \vec{x}_p|\rangle$ is significantly larger than 1 fm as figure 7.2 shows.

In [12] Kachelrieß, Ostapchenko, and Tjemsland (KOT) propose an alternative model for anti-deuteron formation, which is based on a semi-classical description using Wigner-functions and an assumption on the position distribution of the nuclei in the CoM frame. The distribution of the nuclei is assumed to be Gaussian in the CoM frame where the standard deviation is a free parameter of the model. This distribution is shown in figure 7.2 using their best fit value of $\sigma = 1.17$ fm from 7 TeV CoM energy [18]. In this model the distances are on a scale at which coalescence is expected to happen. However, this distribution behaves significantly different than the distribution from the model in `PYTHIA`.

Here a model with a hard cutoff for the position difference of a proton–neutron pair to form a deuteron is studied. This is described in more detail in the next

section.

7.2 Space-Time Coalescence Model

As an alternative model to the standard coalescence model we add an additional coalescence criterion which considers the distance of the neutron and proton in the CoM frame at production. The concept is the same as used for the momenta in the standard coalescence model. There is a hard cutoff where a proton–neutron pair which is close enough in space and momentum space forms a deuteron. This means that

$$|p_n - p_p| < p_0 \quad \text{and} \quad |\vec{x}_n - \vec{x}_p| < x_0, \tag{7.1}$$

must be satisfied.

In this model p_0 is the same as in the standard coalescence model and x_0 is an additional free parameter that must be fitted to experimental data together with p_0. In the momentum part of the coalescence condition p_i are the 4-vectors of the nuclei, while in the position part $\vec{x}_i$ are their 3-vectors at their closest distance in the CoM frame. To get the closest possible distance the formation time of the proton and neutron must be taken into account as well as their directions, which we will discuss in the next section.

7.3 Closest Distance of Proton–Neutron Pairs

In order to find the distance of closest approach of any proton–neutron pair the formation time must be taken into account. The two particles have their respective 4-vectors $x_p = (t_p, \vec{x}_p)$ and $x_n = (t_n, \vec{x}_n)$ at their creation point in space-time in any given reference frame. The particle with the earlier time coordinate must be propagated along its trajectory so the particle positions are compared at the same time. The trajectory is assumed to be a straight line, ignoring the magnetic field in

the detector. This is done by applying the following algorithm to the earlier created nucleus after boosting both nuclei into the CoM frame:

$$\begin{aligned} \Delta t &= T - t, \ t < T, \\ \beta_i &= p_i / E, \\ x_i &\mathrel{+}= \beta_i \Delta t. \end{aligned} \tag{7.2}$$

Here t, T are the ordered time co-ordinates of the neutron and proton, β_i are the velocities of the space components, x_i are the position components of the nucleon and E is the energy. Then after propagating the earlier created particle there are two possible cases which are shown in figure 7.3.

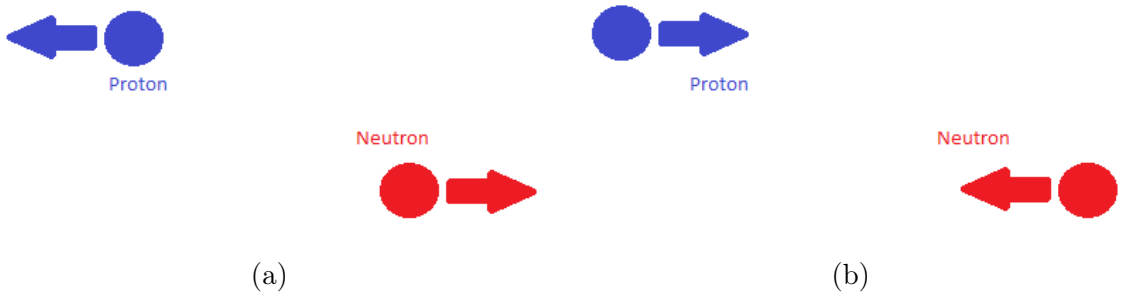

(a) (b)

Figure 7.3: Possible scenarios of a proton–neutron pair in their CoM frame. In (a) the particles move away from each other while in (b) the particles are getting closer.

The particles can either move away from each other or come closer from their creation points. In the first case the closest possible distance is given by the distance after propagating the earlier created particle. In the other case the closest distance is given by the shortest distance between the two trajectories. Since the trajectories are assumed to be straight lines the distance is given by:

$$d = |\hat{n} \cdot (\vec{r}_p - \vec{r}_n)|. \tag{7.3}$$

Here $\hat{n}$ a unit vector normal to both trajectories and $\vec{r}_i$ is an arbitrary point on the trajectory of the particle.

To summarize the algorithm used in this model the following working steps are applied in this alternative coalescence model to every proton–neutron pair:

- Check if the momentum coalescence criterion from eq. (7.1) are satisfied.

- Boost into the CoM frame.

- Propagate the earlier created particle along its trajectory as described in eq. (7.2) to the same time co-ordinate as the later created particle.

- Check if the particles are coming closer or not.

- Calculate the distance of closest approach.

- Check if the space-time coalescence criterion from eq. (7.1) is satisfied.

- If the particles form a deuteron use the same $2 \rightarrow 2$ process kinematics as in the standard coalescence model, described in section 4.3.

Everything not explicitly described here like the kinematics is done in the exact same way as for the standard coalescence model.

7.4 Results

The free parameters x_0 and p_0 have been fitted together to the anti-deuteron measurements from ALICE [24] using weighted input anti-proton and anti-neutron spectra as discussed in section 5.2. Figure 7.4 shows the confidence levels for the best parameter combination based on the resulting χ^2 values.

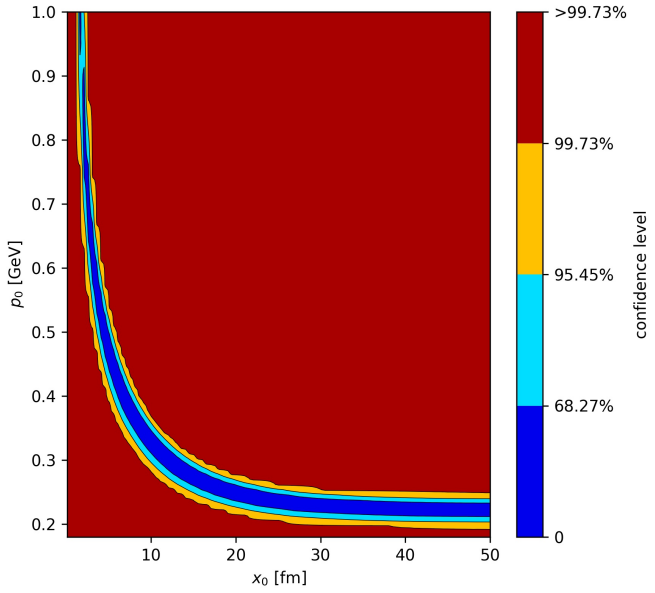

(a) 0.9 TeV

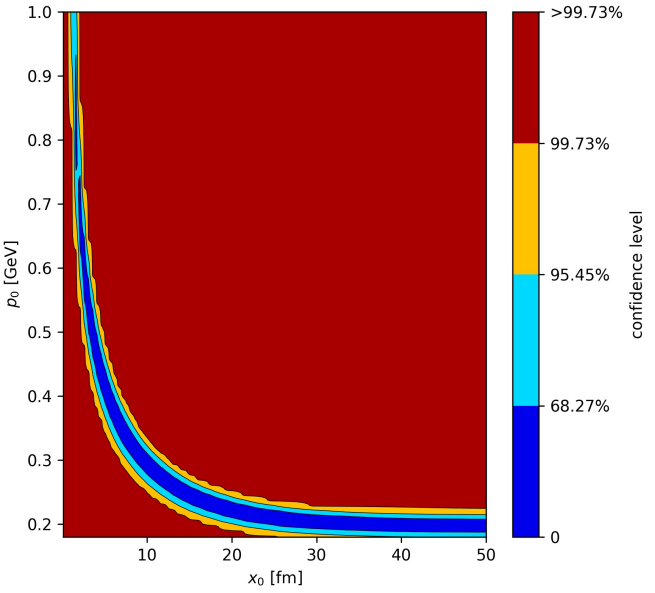

(b) 2.76 TeV

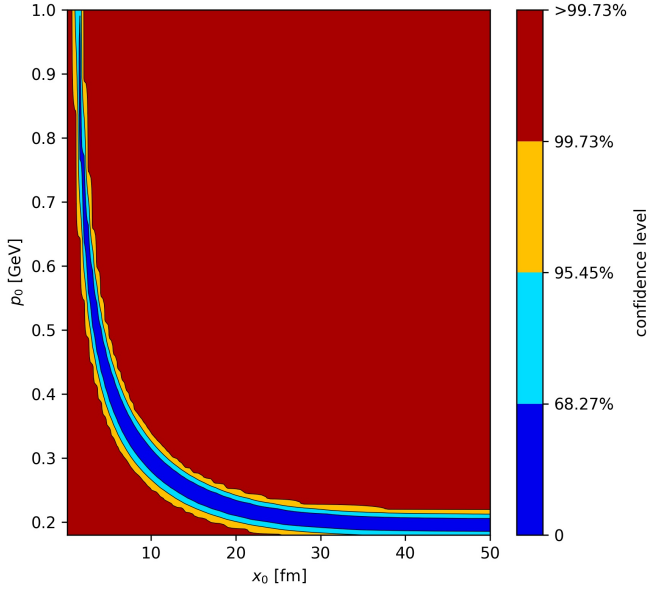

(c) 7 TeV

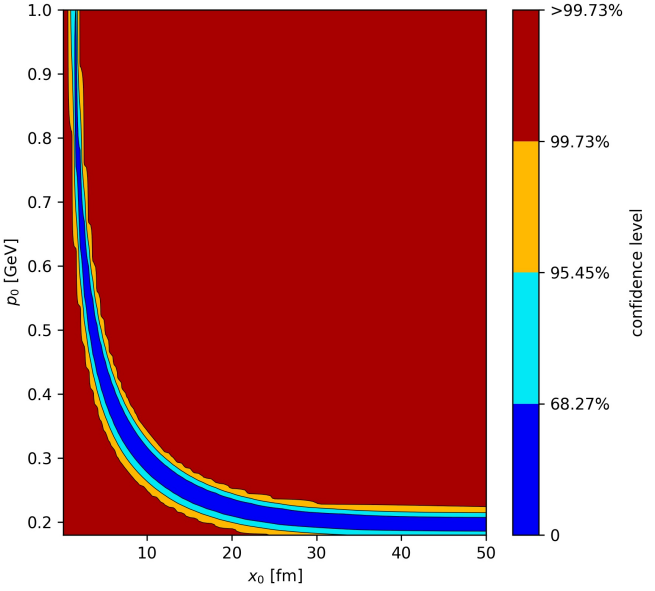

(d) Combined

Figure 7.4: Confidence levels of the free parameters in the space-time model obtained by fitting the anti-deuteron spectra produced by the model to the measurements from ALICE [24].

We can see here that the 1σ range around the best fit values is degenerate for all cases. Therefore a model with an x_0 of $5 \cdot 10^{-12}$ cm, which is unrealistic for coalescence, given the size of the nuclei, would not be excluded by this fit. On the other hand a model with an very high value for p_0 in the order of 1 GeV which is the mass of a proton and much higher than the binding energy of a deuteron, would also not be excluded by this fit. Table 7.1 shows the best fit values for the space-time model from the plots above.

CoM Energy	p_0 [MeV]	x_0 [fm]	χ^2
0.9 TeV	237	24.55	0.20
2.76 TeV	205	28.54	0.15
7 TeV	221	20.56	0.20
combined	229	18.56	0.46

Table 7.1: Best fit values for the free parameters of the alternative coalescence model, for the anti-deuteron spectra from ALICE [24].

The results compared to table 5.3 show that the fits are slightly improved compared to the standard coalescence model and the cross-section model. The resulting values for the best fit for x_0 are between 18 fm and 29 fm, which is just one order of magnitude larger than the size of a nucleon.

Chapter 8

Conclusion

The results of this thesis in chapter 5.2 clearly show that re-weighting the input proton and neutron spectra based on measurements should be done for both the standard coalescence model and the cross-section model. The standard coalescence model is not compatible with the measurements without re-weighting. The cross-section model gives better fits in general, however, without re-weighting the cross-section model is not good enough to explain the measurements. Further improvements on the re-weighting could be done by including weights based on the distribution in rapidity dN/dy, and on correlations of anti-baryon–anti-baryon pairs as the observed anti-correlations might not be well reproduced by MC generators [62]. This is in particular important at low transverse momenta. Also studying the impact of the re-weighting on different CoM energies would be interesting, for example for ALICE measurements at 14 TeV when they become available and also other colliders like LEP.

Studying anti-deuteron formation dependence on event multiplicity classes in chapter 6 showed that only for the mid multiplicity classes can the models provide good fits. For low and high multiplicity the standard coalescence model gives rather poor fits. The cross-section model can explain the multiplicity dependent spectra well for low multiplicity, however, it is unable to describe the anti-deuteron

formation at high multiplicity, especially for the studied spectra at 13 TeV CoM energy. The results showed that for an increasing event multiplicity the coalescence parameters p_0, σ_0^{-1} decreased, which is contrary for our the prior assumption, that the parameters should increase due to a contribution to the anti-deuteron spectra coming from direct hadronization in the fireball. Thus we find no evidence for this production. The decreasing coalescence parameter can possibly be described by models that take into account the size of the fireball, which is the source where the anti-deuterons are created [60].

The space-time model studied in chapter 7 provided slightly improved fits to the measurements compared to the standard coalescence model and cross-section model. While the best fit parameter of the formation length x_0 is between 18 fm and 29 fm, which is only one order of magnitude bigger than the size of a nucleon, and the best fit of p_0 is similar to the standard coalescence model, the fits are degenerated for all studied cases. Since this model allows to take into account the spatial separation of the anti-proton and anti-neutron it would be interesting to study the multiplicity dependent production of anti-deuterons using this model. This would allow to take into account the effect of size of the fireball, which can be related to the event multiplicity [60].

Bibliography

[1] J. H. Oort, *The force exerted by the stellar system in the direction perpendicular to the galactic plane and some related problems*. Bull. Astron. Inst. Netherlands 6, 8, 1932.

[2] F. Zwicky, *Die Rotverschiebung von extragalaktischen Nebeln*. Helv. Phys. Acta 6, 1933.

[3] J. P. Ostriker and P. J. E. Peebles, *A Numerical Study of the Stability of Flattened Galaxies: or, can Cold Galaxies Survive?*, *apj* **186** (Dec., 1973) 467–480.

[4] V. C. Rubin, J. Ford, W. Kent and N. Thonnard, *Extended rotation curves of high-luminosity spiral galaxies. IV. Systematic dynamical properties, Sa through Sc*, *Astrophys. J. Lett.* **225** (1978) L107–L111.

[5] K. Freese, *Review of Observational Evidence for Dark Matter in the Universe and in upcoming searches for Dark Stars*, *EAS Publ. Ser.* **36** (2009) 113–126, [0812.4005].

[6] Planck collaboration, P. A. R. Ade et al., *Planck 2013 results. XVI. Cosmological parameters*, *Astron. Astrophys.* **571** (2014) A16, [1303.5076].

[7] G. Jungman, M. Kamionkowski and K. Griest, *Supersymmetric dark matter*, *Phys. Rept.* **267** (1996) 195–373, [hep-ph/9506380].

[8] Planck collaboration, P. Ade et al., *Planck 2015 results. XIII. Cosmological parameters*, *Astron. Astrophys.* **594** (2016) A13, [1502.01589].

[9] T. Massam, T. Muller, B. Righini, M. Schneegans and A. Zichichi, *Experimental observation of antideuteron production*, *Il Nuovo Cimento A* **63** (Sep, 1965) 10–14.

[10] D. E. Dorfan, J. Eades, L. M. Lederman, W. Lee and C. C. Ting, *Observation of antideuterons*, *Phys. Rev. Lett.* **14** (1965) 1003–1006.

[11] L. A. Dal and A. R. Raklev, *Alternative formation model for antideuterons from dark matter*, *Phys. Rev.* **D91** (2015) 123536, [1504.07242].

[12] M. Kachelrieß, S. Ostapchenko and J. Tjemsland, *Alternative coalescence model for deuteron, tritium, helium-3 and their antinuclei*, *Eur. Phys. J.* **A56** (2020) 4, [1905.01192].

[13] F. Donato, N. Fornengo and P. Salati, *Anti-deuterons as a signature of supersymmetric dark matter*, *Phys. Rev.* **D62** (2000) 043003, [hep-ph/9904481].

[14] M. A. Deliyergiyev, *Recent Progress in Search for Dark Sector Signatures*, *Open Phys.* **14** (2016) 281–303, [1510.06927].

[15] A. Yamamoto et al., *BESS-Polar: Long duration flights at Antarctica to search for primordial antiparticles*, *Nucl. Phys. B Proc. Suppl.* **113** (2002) 208–212.

[16] S. Kenichi, "Search for cosmic-ray antideuterons with bess-polar ii." https://www.icrc2019.org/uploads/1/1/9/0/119067782/icrc2019_ks.pdf.

[17] T. Aramaki et al., *Review of the theoretical and experimental status of dark matter identification with cosmic-ray antideuterons*, *Phys. Rept.* **618** (2016) 1–37, [1505.07785].

[18] M. Kachelriess, S. Ostapchenko and J. Tjemsland, *Revisiting cosmic ray antinuclei fluxes with a new coalescence mode*, 2002.10481.

[19] H. Fuke et al., *Search for cosmic-ray antideuterons*, *Phys. Rev. Lett.* **95** (2005) 081101, [astro-ph/0504361].

[20] A. Kounine, *The Alpha Magnetic Spectrometer on the International Space Station*, *Int. J. Mod. Phys. E* **21** (2012) 1230005.

[21] GAPS collaboration, S. Mognet et al., *The Prototype GAPS (pGAPS) Experiment*, *Nucl. Instrum. Meth. A* **735** (2014) 24–38, [1303.1615].

[22] ALICE collaboration, P. Kuijer, *The Alice experiment at the CERN LHC*, in *31st International Conference on High Energy Physics*, pp. 62–64, 7, 2002.

[23] "CERN website on the ALICE experiment." http://aliceinfo.cern.ch/Public/en/Chapter2/Chap2Experiment-en.html.

[24] ALICE collaboration, S. Acharya et al., *Production of deuterons, tritons, ^{3}He nuclei and their antinuclei in pp collisions at $\sqrt{s}$ = 0.9, 2.76 and 7 TeV*, *Phys. Rev.* **C97** (2018) 024615, [1709.08522].

[25] ALICE collaboration, S. Acharya et al., *Multiplicity dependence of (anti-)deuteron production in pp collisions at $\sqrt{s}$ = 7 TeV*, *Phys. Lett.* **B794** (2019) 50–63, [1902.09290].

[26] ALICE collaboration, S. Acharya et al., *(Anti-)Deuteron production in pp collisions at $\sqrt{s} = 13$ TeV*, 2003.03184.

[27] ALICE collaboration, K. Aamodt et al., *Alignment of the ALICE Inner Tracking System with cosmic-ray tracks*, *JINST* **5** (2010) P03003, [1001.0502].

[28] J. Alme et al., *The ALICE TPC, a large 3-dimensional tracking device with fast readout for ultra-high multiplicity events*, *Nucl. Instrum. Meth. A* **622** (2010) 316–367, [1001.1950].

[29] ALICE collaboration, F. Carnesecchi, *Performance of the ALICE Time-Of-Flight detector at the LHC*, *JINST* **14** (2019) C06023, [1806.03825].

[30] J. Conrad, J. Contreras and C. Jorgensen, *Minimum bias triggers in proton-proton collisions with VZERO and pixel detectors*, 2005.

[31] E. Serradilla, *Producción de núcleos de deuterio y antideuterio en el experimento ALICE del LHC*. PhD thesis, Madrid, CIEMAT, 2013.

[32] ALICE collaboration, B. Abelev et al., *Measurement of inelastic, single- and double-diffraction cross sections in proton–proton collisions at the LHC with ALICE*, *Eur. Phys. J. C* **73** (2013) 2456, [1208.4968].

[33] STAR collaboration, B. I. Abelev et al., *Strange particle production in p+p collisions at $\sqrt{s}$ = 200-GeV*, *Phys. Rev.* **C75** (2007) 064901, [nucl-ex/0607033].

[34] C.-Y. Wong, *Event-by-Event Study of Space-Time Dynamics in Flux-Tube Fragmentation*, *J. Phys.* **G44** (2017) 075102, [1510.07194].

[35] G. Wilk and Z. Wlodarczyk, *Consequences of temperature fluctuations in observables measured in high energy collisions*, *Eur. Phys. J.* **A48** (2012) 161, [1203.4452].

[36] B. Andersson, G. Gustafson, G. Ingelman and T. Sjostrand, *Parton Fragmentation and String Dynamics*, *Phys. Rept.* **97** (1983) 31–145.

[37] C.-Y. Wong and G. Wilk, *Tsallis fits to p_T spectra and multiple hard scattering in pp collisions at the LHC*, *Phys. Rev.* **D87** (2013) 114007, [1305.2627].

[38] T. Sjostrand and P. Z. Skands, *Multiple interactions and the structure of beam remnants*, *JHEP* **03** (2004) 053, [hep-ph/0402078].

[39] R. Hagedorn, *Multiplicities, p_T Distributions and the Expected Hadron $\rightarrow$ Quark - Gluon Phase Transition*, *Riv. Nuovo Cim.* **6N10** (1983) 1–50.

[40] C. Tsallis, *Possible Generalization of Boltzmann-Gibbs Statistics*, *J. Statist. Phys.* **52** (1988) 479–487.

[41] C.-Y. Wong and G. Wilk, *Tsallis Fits to p_T Spectra for pp Collisions at LHC*, *Acta Phys. Polon.* **B43** (2012) 2047–2054, [1210.3661].

[42] G. Wilk and Z. Wlodarczyk, *Multiplicity fluctuations due to the temperature fluctuations in high-energy nuclear collisions*, *Phys. Rev.* **C79** (2009) 054903, [0902.3922].

[43] G. Wilk and Z. Wlodarczyk, *On the interpretation of nonextensive parameter q in Tsallis statistics and Levy distributions*, *Phys. Rev. Lett.* **84** (2000) 2770, [hep-ph/9908459].

[44] J. I. Kapusta, *Mechanisms for deuteron production in relativistic nuclear collisions*, *Phys. Rev.* **C21** (1980) 1301–1310.

[45] L. Landau and E. Lifshitz, *Quantum Mechanics: Non-relativistic Theory*, *Butterworth-Heinemann* (1977) .

[46] D. Belkic, *Principles of Quantum Scattering Theory*. Boca Raton: CRC Press, 2003.

[47] J. Bystricky, P. La France, F. Lehar, F. Perrot, T. Siemiarczuk and P. Winternitz, *Energy Dependence of Nucleon-Nucleon Inelastic Total Cross-Sections*, 1987.

[48] H. Machner and J. Niskanen, *Charge independence studied in NN —> d pi reactions*, *Nucl. Phys.* **A776** (2006) 172–188, [nucl-ex/0511027].

[49] Particle Data Group collaboration, M. Tanabashi et al., *Review of Particle Physics*, *Phys. Rev.* **D98** (2018) 030001.

[50] T. Sjöstrand, S. Ask, J. R. Christiansen, R. Corke, N. Desai, P. Ilten et al., *An Introduction to PYTHIA 8.2*, *Comput. Phys. Commun.* **191** (2015) 159–177, [1410.3012].

[51] T. Sjostrand, S. Mrenna and P. Z. Skands, *PYTHIA 6.4 Physics and Manual*, *JHEP* **05** (2006) 026, [hep-ph/0603175].

[52] ALICE collaboration, S. Acharya et al., *Multiplicity dependence of π, K, and p production in pp collisions at $\sqrt{s} = 13$ TeV*, 2003.02394.

[53] ALICE collaboration, K. Aamodt et al., *Production of pions, kaons and protons in pp collisions at $\sqrt{s} = 900$ GeV with ALICE at the LHC*, *Eur. Phys. J. C* **71** (2011) 1655, [1101.4110].

[54] ALICE collaboration, J. Adam et al., *Measurement of pion, kaon and proton production in proton–proton collisions at $\sqrt{s} = 7$ TeV*, *Eur. Phys. J. C* **75** (2015) 226, [1504.00024].

[55] ALICE collaboration, *The ALICE definition of primary particles*, Jun, 2017.

[56] ALICE collaboration, J. Adam et al., *Enhanced production of multi-strange hadrons in high-multiplicity proton-proton collisions*, *Nature Phys.* **13** (2017) 535–539, [1606.07424].

[57] ALICE collaboration, B. Abelev et al., *J/ψ Production as a Function of Charged Particle Multiplicity in pp Collisions at $\sqrt{s} = 7$ TeV*, *Phys. Lett. B* **712** (2012) 165–175, [1202.2816].

[58] ALICE collaboration, S. Acharya et al., *Multiplicity dependence of light-flavor hadron production in pp collisions at $\sqrt{s} = 7$ TeV*, *Phys. Rev. C* **99** (2019) 024906, [1807.11321].

[59] ALICE collaboration, S. Acharya et al., *Multiplicity dependence of (multi-)strange hadron production in proton-proton collisions at $\sqrt{s} = 13$ TeV*, *Eur. Phys. J. C* **80** (2020) 167, [1908.01861].

[60] F. Bellini and A. P. Kalweit, *Testing production scenarios for (anti-)(hyper-)nuclei and exotica at energies available at the CERN Large Hadron Collider*, *Phys. Rev. C* **99** (2019) 054905, [1807.05894].

[61] S. Ferreres-Solé and T. Sjöstrand, *The space–time structure of hadronization in the Lund model*, *Eur. Phys. J.* **C78** (2018) 983, [1808.04619].

[62] ALICE collaboration, J. Adam et al., *Insight into particle production mechanisms via angular correlations of identified particles in pp collisions at* $\sqrt{s} = 7$ *TeV*, *Eur. Phys. J. C* **77** (2017) 569, [1612.08975].